

UNIVERSITY OF SÃO PAULO  
SÃO CARLOS SCHOOL OF ENGINEERING

**Gabriela Mayumi de Freitas Otsubo**

**Effects of piezoelectric based nonlinear energy sink on the  
aeroelastic behavior of a typical section**

São Carlos-SP

2020



**Gabriela Mayumi de Freitas Otsubo**

**Effects of piezoelectric based nonlinear energy sink on the  
aeroelastic behavior of a typical section**

Dissertation submitted to São Carlos School of Engineering, University of São Paulo, as one of the requisites for obtaining the degree of Master in Sciences - Graduate Program of Mechanical Engineering.

Concentration Area: Aeronautics

Advisor: Prof. Dr. Carlos De Marqui Junior

São Carlos-SP

2020

I AUTHORIZE TOTAL OR PARTIAL REPRODUCTION OF THIS WORK BY ANY CONVENTIONAL OR ELECTRONIC MEANS, FOR RESEARCH PURPOSES, SO LONG AS THE SOURCE IS CITED.

Ficha catalográfica elaborada pela Biblioteca Prof. Dr. Sérgio Rodrigues Fontes da EESC/USP com os dados inseridos pelo(a) autor(a).

D112e de Freitas Otsubo, Gabriela Mayumi  
Effects of piezoelectric based nonlinear energy sink on the aeroelastic behavior of a typical section / Gabriela Mayumi de Freitas Otsubo; orientador Carlos De Marqui Jr. São Carlos, 2020.

Dissertação (Mestrado) - Programa de Pós-Graduação em Engenharia Mecânica e Área de Concentração em Aeronáutica -- Escola de Engenharia de São Carlos da Universidade de São Paulo, 2020.

1. Nonlinear Energy Sink. 2. Aeroelastic Control.  
3. Piezoelectricity. I. Título.

## **Abstract**

DE FREITAS OTSUBO, G. M. **Effects of piezoelectric based nonlinear energy sink on the aeroelastic behavior of a typical section.** 2020. 86p. Dissertation (Master) - São Carlos School of Engineering, University of São Paulo, São Carlos, 2020.

The attenuation of undesired structural vibrations is of interest in a variety of engineering applications ranging from industrial machines to aerospace structures. Especially for lightweight and flexible structures used in aircraft and spacecraft systems, piezoelectric shunt damping offers remarkable advantages as an electronic damping approach without the mass loading effects of conventional and bulky vibration damping methods. Linear piezoelectric vibration absorbers are tuned to a specific frequency and, therefore, their control performance may be significantly reduced if the target frequency is modified due to variation of environmental conditions, fabrication tolerances, parameter uncertainties, or nonlinearities, among others. Researchers have explored different types of nonlinear piezoelectric shunt circuits to enhance the vibration suppression bandwidth of piezoelectric absorbers and, therefore, overcome the limitations of linear piezoelectric absorbers. This work extends this topic by investigating numerically and experimentally the influence of nonlinear piezoelectric vibration absorbers on the behavior of linear and nonlinear aeroelastic systems. A typical section with two degrees of freedom is used and the electromechanical coupling is added to the plunge degree of freedom. Later, a concentrated nonlinearity, free play, is added to the typical section. For each typical section, the short-circuit configuration is assumed as reference case and the increase in the flutter speed is obtained numerically and experimentally. The results are presented in time and frequency domain and show increases of flutter speed from 2.5 % for the experimental nonlinear typical section to 3.7 % for the experimental linear one.

**Keywords:** Nonlinear Energy Sink. Aeroelastic Control. Piezoelectricity.



## **Resumo**

DE FREITAS OTSUBO, G. M. **Efeito de absorvedores piezelétricos de vibração não-lineares sobre o comportamento aeroelástico de uma seção.** 2020. 86p. Dissertação (Mestrado) – Escola de Engenharia de São Carlos, Universidade de São Paulo, São Carlos, 2020.

A atenuação de vibrações estruturais indesejadas é de interesse em uma variedade de aplicações de engenharia, desde máquinas industriais até estruturas aeroespaciais. Principalmente no caso estruturas leves e flexíveis usadas em sistemas de aeronaves e espaçonaves, o shunt damping piezelétrico oferece vantagens notáveis, como uma abordagem de amortecimento eletrônico minimizando a adição de massa e de volume dos métodos convencionais de amortecimento de vibração. Absorvedores de vibração piezoelétricos lineares são sintonizados para uma frequência específica e, portanto, seu desempenho pode ser reduzido significativamente se a frequência alvo for modificada devido à variação das condições ambientais, tolerâncias de fabricação, incertezas de parâmetro, não-linearidades, entre outros. Pesquisadores exploraram diferentes tipos de circuitos shunt damping piezelétricos não-lineares para aumentar a faixa de frequências de operação e, portanto, superar as limitações dos absorvedores piezoelétricos lineares. Este trabalho estende este tópico investigando numericamente e experimentalmente a influência de absorvedores de vibração piezelétricos não-lineares no comportamento de sistemas aeroelásticos lineares e não-lineares. Uma seção típica com dois graus de liberdade é utilizada e o acoplamento eletromecânico é adicionado no grau de liberdade de plunge. Depois uma não-linearidade concentrada, free play, é adicionada à seção típica. Para cada seção, a configuração de curto-circuito é usada como caso de referência e o aumento da velocidade de flutter devido ao NES é obtido numericamente e experimentalmente. Os resultados são mostrados no domínio do tempo e da frequência e mostram aumentos na velocidade de flutter variando de 2,5 % para a seção típica não-linear experimental até 3,7 % para a linear experimental.

**Palavras-chave:** Nonlinear Energy Sink. Controle Aeroelástico. Piezeletricidade.



## List of Figures

Figure 2.1 Nonlinear resonance (VAKAKIS et al., 2008) .....	23
Figure 2.2 Model and experimental setup of the proposed rotating NES (AL-SHUDEIFAT et al., 2017).....	24
Figure 2.3 Model used in the numerical work of Lee and co-authors (LEE et al., 2007b) .....	25
Figure 2.4 Mechanical NES used in the experimental work of Lee and co-authors (LEE et al., 2007a) .....	25
Figure 2.5 Rotating NES (HUBBARD et al., 2010) .....	26
Figure 2.6 Nonlinear shunt (VIGUIÉ; KERSCHEN; RUZZENE, 2009) .....	26
Figure 2.7 Single degree of freedom system of a mass and a piezoelectric element (ZHOU; THOUVEREZ; LENOIR, 2014) .....	27
Figure 3.1 Aeroelastic typical section model .....	29
Figure 3.2 Restoring moments in the pitch DOF for the linear and the free play configurations .....	32
Figure 3.3 Equivalent electrical circuit for a 2-DOF aeroelastic typical section .....	35
Figure 3.4 Voltage-controlled (a) and current-controlled (b) voltage source from MatLab Simulink.....	37
Figure 3.5 Equivalent electrical circuit for a 2-DOF aeroelastic typical section with NES .....	38
Figure 3.6 Pitch equivalent electrical circuit with free play .....	39
Figure 4.1 Mechanical NES applied to the plunge DOF of the typical section .....	40
Figure 4.2 Electrical NES .....	41
Figure 4.3 Nonlinear energy sink circuit with negative capacitance (red) and cubic nonlinearity (blue) .....	42
Figure 4.4 Negative capacitance circuit schematic .....	42
Figure 4.5 Negative capacitance circuit .....	43
Figure 4.6 $G_1$ circuit .....	44
Figure 4.7 $G_2$ circuit (differential amplifier) .....	45
Figure 4.8 $G_3$ circuit .....	46
Figure 5.1 NES block diagram .....	48
Figure 5.2 Discrete operational amplifier.....	49

Figure 5.3 High-voltage operational amplifier experiment .....	49
Figure 5.4 Blower wind tunnel .....	50
Figure 5.5 Two degree of freedom typical section during wind tunnel tests .....	51
Figure 5.6 Connection of the typical section to the fixed support – lower end.....	51
Figure 5.7 Pitch detail – upper end.....	52
Figure 5.8 Piezoceramics.....	52
Figure 5.9 Simulation flow chart.....	54
Figure 5.10 Numerical time responses of pitch and plunge displacements at airflow speeds around the numerical short-circuit flutter speed (9.8 m/s) for the linear typical section at SC condition .....	55
Figure 5.11 Numerical and experimental time responses of pitch and plunge displacements at the correspondent short-circuit flutter speed (9.8 m/s for the numerical and 10.8 m/s for the experimental) for the linear typical section at SC condition .....	56
Figure 5.12 Numerical and experimental time responses of pitch and plunge displacements at (a) 3.9 m/s, (b) 6.7 m/s, (c) 8.9 m/s and (d) 9.5 m/s for the linear typical section at SC condition .....	56
Figure 5.13 Voltage-charge behavior for the linear typical section with NES.....	59
Figure 5.14 Nonlinear voltage-charge behavior for the linear typical section with NES .....	59
Figure 5.15 Numerical effects of piezoelectric NES at numerical short-circuit (SC) flutter speed (9.8 m/s) for pitch and plunge displacements, the voltage across the piezoelectric material and the cubic voltage for the linear typical section.....	60
Figure 5.16 Numerical time responses of pitch and plunge displacements, the voltage across the piezoelectric material and the cubic voltage at airflow speeds around the numerical flutter speed (10.1 m/s) for the linear typical section with NES .....	61
Figure 5.17 Numerical and experimental time responses of pitch and plunge displacements, the voltage across the piezoelectric material and the cubic voltage at the correspondent flutter speed (10.1 m/s for the numerical and 11.2 m/s for the experimental) for the linear typical section with NES .....	62
Figure 5.18 Numerical and experimental wavelet transform at the correspondent flutter speed (10.1 m/s for the numerical and 11.2 m/s for the experimental) for the linear typical section with NES .....	63
Figure 5.19 Input energy, dissipated energy and energy in the system at numerical short-circuit flutter speed (9.8 m/s).....	65

Figure 5.20 Power flowing from the mechanical to the electrical domain for at numerical short-circuit flutter speed (9.8 m/s) .....	65
Figure 5.21 Flutter speed against the factor $\gamma$ .....	66
Figure 6.1 Numerical time responses of pitch and plunge displacements at airflow speeds around the numerical range of LCO for the nonlinear typical section at SC condition .....	68
Figure 6.2 Numerical and experimental nonlinear time responses of pitch and plunge displacements at the speed above which LCO is observed (9.5 m/s for the numerical and 11.0 m/s for the experimental) for the nonlinear typical section.....	68
Figure 6.3 Numerical effects of piezoelectric NES at 9.5 m/s for pitch and plunge displacements, the voltage across the piezoelectric material and the cubic voltage for the nonlinear typical section.....	69
Figure 6.4 Numerical time responses of pitch and plunge displacements, the voltage across the piezoelectric material and the cubic voltage at airflow speeds around the stability boundary (9.9 m/s) for the nonlinear typical section.....	70
Figure 6.5 Numerical and experimental time responses of pitch and plunge displacements, the voltage across the piezoelectric material and the cubic voltage at the boundary stability speed (9.9 m/s for the numerical and 11.3 m/s for the experimental) for the nonlinear typical section .....	71
Figure 6.6 Numerical and experimental wavelet transform at the correspondent flutter speed (9.9 m/s for the numerical and 11.3 m/s for the experimental) .....	72
Figure 6.7 Input energy, dissipated energy and energy in the system at numerical short-circuit flutter speed (9.5 m/s).....	73
Figure 6.8 Power flowing from the mechanical to the electrical domain for at numerical short-circuit flutter speed (9.5 m/s) .....	73
Figure A.0.1 Plunge Stiffness.....	83
Figure A.0.2 Pitch Stiffness.....	83
Figure A.0.3 Plunge Damping.....	85
Figure A.0.4 Pitch Damping.....	85

## **List of Tables**

Table 1. Electrical elements.....	36
Table 2. Electrical sources.....	38
Table 3. High-voltage operational amplifier parameters.....	50
Table 4. Typical section parameters .....	53
Table 5. Maximum design voltages.....	58
Table 6. NES final parameters.....	58
Table 7. Comparison between speeds prediction .....	74
Table 8. Beam parameters .....	83



## List of Symbols

$a$	Distance of the axis of rotation from the mid-chord per semichord
$B_h$	Damping coefficient per length for the plunge DOF
$B_{NES}$	Mechanical nonlinear energy sink damping
$B_\alpha$	Damping coefficient per length for the pitch DOF
$b$	Semichord
$b_{beam}$	Base of the beam section
$C(k)$	Theodorsen's function
$C_h$	Plunge capacitor
$C_{neg}$	Negative capacitance
$C_{nl}$	Nonlinear capacitance
$C_p$	Equivalent capacitance of the piezoelectric material
$C_{res}$	Equivalent (residual) capacitance
$C_2$	Capacitor of negative capacitance circuit
$C_\alpha$	Pitch capacitor
$CS_n$	Controlled source - subscript $n$ varies from 1 to 8
$c_n$	Coupling term - subscript $n$ can be equal to 2, 3 5 or 6
$E$	Electrical energy per length
$ED$	Dissipated energy
$E_{in}$	Input energy
$E_{sis}$	Total energy of the system
$F$	Aerodynamic lift per length
$F_h, \dot{F}_h, F_\alpha, \dot{F}_\alpha$	Nondimensional oscillatory aerodynamic derivatives related to lift
$f_{fp}$	Free play restoring moment
$f_n$	Natural frequency of oscillation in Hz
$f_{nl}$	Generic nonlinear restoring moment
$G_n$	Circuit gain - subscript $n$ varies from 1 to 3
$g$	Gravity acceleration
$h$	Plunge displacement
$h_i$	Initial plunge displacement
$h_0$	Amplitude of harmonic motion for plunge
$h_{beam}$	Height of the beam section

$I_{CG}$	Mmoment of inertia per length about the center of gravity
$I_z$	Moment of inertia of the beam
$I_\alpha$	Moment of inertia per length about the elastic axis
$i$	Complex number
$K$	Kinetic energy per length
$K_{beam}$	Beam stiffness
$K_h$	Stiffness per length for the plunge DOF
$K_{NES}$	Mechanical nonlinear energy sink stiffness
$K_\alpha$	Stiffness per length for the pitch DOF
$k$	Reduced frequency
$k_n$	Integral constant - subscript $n$ varies from 1 to 4
$L$	NES inductor
$L_{beam}$	Length of the beam
$L_h$	Plunge inductor
$L_\alpha$	Pitch inductor
$l$	Span length
$M$	Aerodynamic moment per length
$M_h, M_{\dot{h}}, M_\alpha, M_{\dot{\alpha}}$	Nondimensional oscillatory aerodynamic derivatives related to moment
$M_z$	Bending moment of the beam
$m$	Airfoil mass per length
$m_f$	Fixture mass per length
$m_{f\ damp}$	Mass of the device used to lock the pitch DOF
$m_{NES}$	Mechanical nonlinear energy sink mass
$P$	Potential energy per length
$P_h$	Energy flow from the mechanical to the electrical domain
$P_y$	External force of the beam
$Q$	Dissipation function per length
$q_p$	NES electrical charge
$q_n$	Electrical charge - subscript $n$ varies from 1 to 5
$R$	NES resistor
$R_h$	Plunge resistor
$R_n$	Resistor - subscript $n$ varies according circuit

$R_\alpha$	Pitch resistor
$S_\alpha$	Static moment
$T_\alpha$	Period of oscillation
$t$	Time
$U$	Airflow speed
$u$	General displacement
$u_y$	Transversal displacement of the beam
$V_{dd}$	Positive power supply voltage (operational amplifier)
$V_{in}$	Input voltage
$V_n$	Voltage - subscript $n$ varies according circuit
$V_{out}$	Output voltage
$V_p$	Voltage across the shunted circuit
$V_{ss}$	Negative power supply voltage (operational amplifier)
$V_y$	Shear force of the beam
$W_{NC}$	Nonconservative work
$x$	Coordinate system
$x_{CG}$	Horizontal coordinate of the center of gravity
$x_\alpha$	Distance of the axis of rotation from the center of gravity per semichord
$Y$	Young modulus
$y_{CG}$	Vertical coordinate of the center of gravity
$\alpha$	Pitch angle
$\alpha_0$	Amplitude of harmonic motion for pitch
$\alpha_{fp}$	Semi free play gap
$B$	Nondimensional parameter related to the nonlinear capacitance
$\gamma$	Multiplicative factor
$\theta$	Electromechanical coupling
$\theta_z$	Rotation of the beam section
$\xi$	Damping factor
$\xi_h$	Plunge damping factor
$\xi_\alpha$	Pitch damping factor
$\rho$	Density of the fluid
$\omega$	Frequency of oscillation in rad/s

$\omega_n$

Natural frequency of oscillation in rad/s

# Content

<b>1</b>	<b>Introduction .....</b>	<b>17</b>
<b>2</b>	<b>Literature Review .....</b>	<b>21</b>
2.2	Linear Piezoelectric Absorbers .....	21
2.3	Nonlinear Piezoelectric Absorbers .....	22
<b>3</b>	<b>Typical Section Equivalent Electrical Model .....</b>	<b>29</b>
3.1	Typical Section Equations of Motion .....	29
3.1.1	Nonlinear Typical Section .....	31
3.1.2	Aerodynamic Loads.....	32
3.2	Equivalent Electrical Model .....	35
3.2.1	Nonlinear Equivalent Electrical Model .....	38
<b>4</b>	<b>Nonlinear Energy Sink .....</b>	<b>40</b>
4.1	Proposed Nonlinear Energy Sink Circuit.....	41
<b>5</b>	<b>Effects of Piezoelectric Based NES on the Aeroelastic Behavior of the Linear Typical Section .....</b>	<b>48</b>
5.2	Evaluation of Voltage Magnitudes Of The Piezoelectric Material.....	48
5.3	Description of the Experimental Apparatus and Simulation Procedure .....	50
5.4	Reference Case .....	54
5.5	Linear Typical Section Combined to the Nonlinear Shunt Circuit.....	57
<b>6</b>	<b>Effects of Piezoelectric Based NES on the Aeroelastic Behavior of the Nonlinear Typical Section .....</b>	<b>67</b>
6.2	Reference Case .....	67
6.3	Nonlinear Typical Section Combined to the Nonlinear Shunt Circuit .....	69
<b>7</b>	<b>Conclusions .....</b>	<b>75</b>
<b>8</b>	<b>References .....</b>	<b>77</b>
	<b>Appendix A - Identification of Typical Section Parameters.....</b>	<b>81</b>

## 1 Introduction

The classical aeroelasticity literature reports and discusses different static and dynamic aeroelastic phenomena (BISPLINGHOFF; ASHLEY; HALFMAN, 1996; DOWELL, 2015; HODGES; PIERCE; CUTCHINS, 2003; THEODORSEN, 1935). Flutter, a dynamic aeroelastic phenomenon related to interactions of inertial, elastic and aerodynamic forces, is certainly the most investigated one due to its catastrophic nature. When a linear aeroelastic system is considered, the system is stable for airflow speeds smaller than the linear flutter speed (or critical speed) and any further increase in the airflow speed leads to instability: self-sustained aeroelastic oscillations with increasing amplitude. However, nonlinearities are often present in aeroelastic systems in the forms of concentrated nonlinearities (free play or bilinear stiffness due to loosely connected components), structural nonlinearities (due to large motions, material nonlinearities, and dissipation-related behaviors), geometric nonlinearity (typically yielding nonlinear stiffness effect) and aerodynamic nonlinearities (stall effects, transonic effects).

Nonlinear systems, including aeroelastic ones, present a very rich variety of dynamic behavior, such as limit cycle oscillations (LCOs), internal resonances, and chaotic motions (MOON, 1985; NAYFEH; MOOK, 1985). Several papers in the literature explore the modeling of concentrated nonlinearities in airfoil sections with different numbers of DOFs. DOWELL and TANG (2002) report two possible general consequences of any nonlinear effect. First, unstable linear behavior beyond the linear flutter speed is converted to limit cycle oscillations (LCO), which is a benign behavior, although LCOs of large amplitudes can be achieved. Second, the system originally stable to small perturbations can become unstable due to large disturbances, which means LCO can occur for airflow speeds smaller than the linear critical one. Several authors have investigated the nonlinear aeroelastic behavior of airfoil sections with concentrated nonlinearities (DOWELL; TANG, 2002). Although the configuration is quite simple, the fundamental physical phenomena are clearly represented.

Traditionally, the attenuation of undesired aeroelastic vibrations includes techniques such as mass balance and structural reinforcement. In the first case, the goal is to reduce the offset between center of mass of a lifting surface and the elastic axis (or the offset between the center of mass and hinge line of a control surface). In the second case, additional stiffness is added to the structure through reinforcement elements.

Although both techniques improve the aeroelastic behavior, they also introduce significant weight penalties. In this regard, modern strategies considering smart materials have been pointed out in the literature as topics that deserve investigation.

Smart material can be defined as a class of material with properties that couple different physical domains, in other words, when subjected to some external stimuli corresponding to a specific physical domain, these materials respond by varying properties corresponding to another domain (LEO, 2007). In this regard, piezoelectric materials are those that exhibit coupling between mechanical and electrical domain. They produce an electrical output when subjected to mechanical strain, phenomenon called “direct effect” and demonstrated first for some natural materials by the Curie brothers in 1880. In 1881, the reciprocal effect, “inverse effect”, was mathematically demonstrated by Gabriel Lippmann and experimentally confirmed by the Curie brothers. However, due to the weak coupling exhibited by the materials the electrical outputs were relatively small and only in the twentieth century the synthetic piezoelectric materials allowed practical applications.

Piezoelectric materials have been investigated for the attenuation of undesired structural vibrations in a variety of engineering applications ranging from experimental beam setups (HAGOOD; VON FLOTOW, 1991) to aircraft panels (HAGOOD; CRAWLEY, 1991; WU, 2000) and space truss structures (HAGOOD; CRAWLEY, 1991), offering remarkable advantages especially for lightweight flexible structures used in aircraft and spacecraft systems (AHMADIAN; DEGUILIO, 2001; LESIEUTRE, 1998), as the minimization of mass loading and volume of conventional vibration damping methods (JONES, 2001; NASHIF et al., 1985). ABDELKEFI (2016) presents a review of the field of energy harvesting from aeroelastic vibrations, with various types of aeroelastic vibration mechanisms and representative mathematical models.

Piezoelectric shunt damping is applied by connecting a linear electrical circuit to the electrode terminals of a piezoelectric interface that is attached to the main structure. Mechanical energy is converted to electrical energy by the direct effect of the piezoelectrical material and is dissipated on the external circuit. Various types and applications of piezoelectric shunt damping can be found in review articles by AHMADIAN and DEGUILIO (2001) and LESIEUTRE (1998). Resistive, capacitive,

inductive, and resistive-inductive shunt circuits are the typical linear shunt concepts (LESIEUTRE, 1998).

Piezoelectric shunt circuits, as a linear vibration absorber, may have its performance reduced if the target frequency of operation is modified. To overcome this limitation, one of the alternatives is the nonlinear vibration absorbers, which includes the Nonlinear Energy Sinks (NES), an essentially nonlinear device that, under certain conditions, offers nonlinear energy pumping or targeted energy transfer (GENDELMAN, 2001; GENDELMAN et al., 2001; VAKAKIS et al., 2008; VAKAKIS; GENDELMAN, 2001). This phenomenon consists in energy flowing only from the host structure to the device, where can be dissipated in a resistor or, in case of a mechanical version, in a damper. The first studies focus on developing mechanical versions of the NES, however, in most cases, obtaining the essentially nonlinear behavior proved to be a challenge and results in complex structures that requires a significant installation space. That is why the piezoelectric based NES has been the subject of several studies (VIGUIÉ; KERSCHEN; RUZZENE, 2009; ZHOU; THOUVEREZ; LENOIR, 2014), including this one. Besides the publications from our research group (SILVA et al., 2018; SILVA; CLEMENTINO; DE MARQUI, 2018), the device used in this work is based on the mechanical configuration presented by Lee and his coauthors (LEE et al., 2007a, 2007b), and the circuit presented by ZHOU, THOUVEREZ and LENOIR (2014), that allows the implementation of the electrical version of the device.

Our research group has recently proposed an essentially nonlinear piezoelectric shunt circuit for the practical realization of the piezoelectric based nonlinear energy sink (SILVA; CLEMENTINO; DE MARQUI, 2018). The device was attached on a cantilever beam and its performance was verified. In this work, the goal is to investigate numerically and experimentally the performance of the nonlinear piezoelectric based device for aeroelastic control. For that, a linear and a nonlinear typical section with two degrees of freedom is used. The simulate both typical sections, equivalent circuit models (ELVIN, 2014) are used. As the entire system is represented in the electrical domain, all simulations presented can be exclusively performed in circuit simulation softwares. The first step is to obtain the mathematical modeling of the typical sections using Theodorsen's theory to calculate the aerodynamical loads. Then the correspondent equivalent electrical models are obtained, concluding the representation of the host

structure, in which the piezoelectric based NES is attached. Then the device proposed by our research group (SILVA et al., 2018; SILVA; CLEMENTINO; DE MARQUI, 2018) is presented.

Later, preliminary numerical analyses are performed to evaluate voltage magnitudes across the piezoelectric material and the piezoelectric NES is adapted to the aeroelastic structure. The numerical analyses with the final configuration are performed for the linear typical section without and with the piezoelectric NES (short circuit condition is assumed as a reference case). The effects of the device are verified in terms of flutter speed and the system response are obtained in time and frequency domain (wavelet transforms). The results are then verified with wind tunnel experiments. Finally, a concentrated nonlinearity is added to the pitch degree of freedom and the procedure is repeated.

## 2 Literature Review

### 2.2 Linear Piezoelectric Absorbers

Piezoelectric shunt damping represents one of the earliest efforts to develop a vibration control device based on piezoelectric materials. LESIEUTRE (1998) presents a review on shunted piezoelectric materials, in which, the typical ones are identified as the resistive, capacitive, inductive and resistive-inductive circuits. The resistive shunting concept was first used by UCHINO and ISHII (1988) and a significant variation in damping factor is realized when the resistance is changed. Another effect is the variation of the system stiffness since elastic properties of the piezoelectric material depends on the electrical boundary conditions. Capacitive shunting results in a variation of structural stiffness with changing external capacitance (LESIEUTRE, 1998). Changing structural stiffness alters the resonance frequencies of the structure but damping is not affected. Inductive shunting was first studied by FORWARD (1979) and it was shown that the inductance can be selected to cancel the internal piezoelectric capacitance, yielding an undamped dynamic vibration absorber effect. Knowing from UCHINO and ISHII (1988) that a resistor could be used to create damping effect, HAGOOD and VON FLOTOW (1991) connected a resistor and inductor in series to realize the damped dynamic vibration absorber effect. WU (1996) proposed connecting the resistor and inductor in parallel as an alternative resistive-inductive shunt circuit. The result is again a damped dynamic vibration absorber (or a piezoelectric vibration absorber) but the damping trend with changing shunt resistance is reversed as compared to series connection. The resistive-inductive shunt circuits (series and parallel) have received the most attention (LESIEUTRE, 1998) as they create the damped dynamic vibration absorber effect with proper selection of inductance and resistance. One of the firsts studies that applied a piezoelectric absorber to aeroelastic systems presented a procedure for a modal-based modeling of shunted piezoelectric devices applied to several structures, from a cantilever beam to a unmanned glider (AGNENI; MASTRODDI; POLLI, 2003). The performance of shunted piezoelectrics to reduce the aeroelastic response of a 2-DOF typical airfoil section has also been investigated (MCGOWAN, 1999). In both cases, the authors report that passive shunt damping

circuits can significantly reduce the aeroelastic response below the linear flutter speed, although the flutter boundary is not modified.

Linear piezoelectric vibration absorbers, such as the resistive-inductive circuits previously cited, are tuned to a specific frequency. Different tuning rules were proposed in the literature (HAGOOD; VON FLOTOW, 1991; YAMADA et al., 2010). As a result, their control performance may be significantly reduced if the target frequency is modified due to variations of environmental conditions (e.g. temperature), fabrication tolerances, parameter uncertainties, or nonlinearities, among others.

To overcome this limitation, Dell'Isola and his co-authors (ALESSANDRONI et al., 2005; ALESSANDRONI et al., 2002; ANDREAUS; DELL'ISOLA, 2004) investigated the multimodal damping of continuous electroelastic systems by distributing piezoelectric elements that are interconnected to a single passive circuit by leveraging the principle of similarity. Dell'Isola and his co-authors demonstrated that when principle of similarity is respected, or the electric controller is governed by the same equations of the mechanical structure, a multiresonant coupling is accomplished assuring a substantial energy transfer for any initial condition. Multi-modal damping using piezo patches has also been investigated in a aeroelastic case, in which the device demonstrated few improvement on the stability margin of an unmanned glider wing, although it was able to reduce the amplitude of the gust response (AGNENI et al., 2006).

On another research front to enhance the vibration suppression bandwidth of piezoelectric absorbers, researchers have explored different types of nonlinear piezoelectric shunt circuits, which are presented in the next section.

### **2.3 Nonlinear Piezoelectric Absorbers**

SOLTANI and KERSCHEN (2015) explored the effects of a piezoelectric vibration absorber designed to attenuate vibrations of a nonlinear primary system. The device was termed as nonlinear piezoelectric tuned vibration absorber (NPTVA) because its nonlinear restoring force should respect the principle of similarity (HABIB; KERSCHEN, 2016), which means the NPTVA is designed to be an electrical analog of the nonlinear main system. In another work (HABIB et al., 2015), they extended the equal-peak method developed by DEN HARTOG (1985) for mechanical absorbers to nonlinear systems to tune the nonlinear piezoelectric vibration absorber according to the nonlinear elastic characteristics of a host structure.

Some researchers have focused on a specific type of nonlinear piezoelectric absorber, which is based on the nonlinear energy sink (NES) concept (VAKAKIS et al., 2008). Although the focus of this work is piezoelectric version of this device, the first studies presented mechanical versions, which were applied even in aeroelastic cases, as the version displayed in Figure 2.1. A NES and is an essentially nonlinear attachment, with purely nonlinear stiffness element. The absence of linear stiffness term results in a system with no preferential resonance frequency, therefore no tuning is required during the design process.

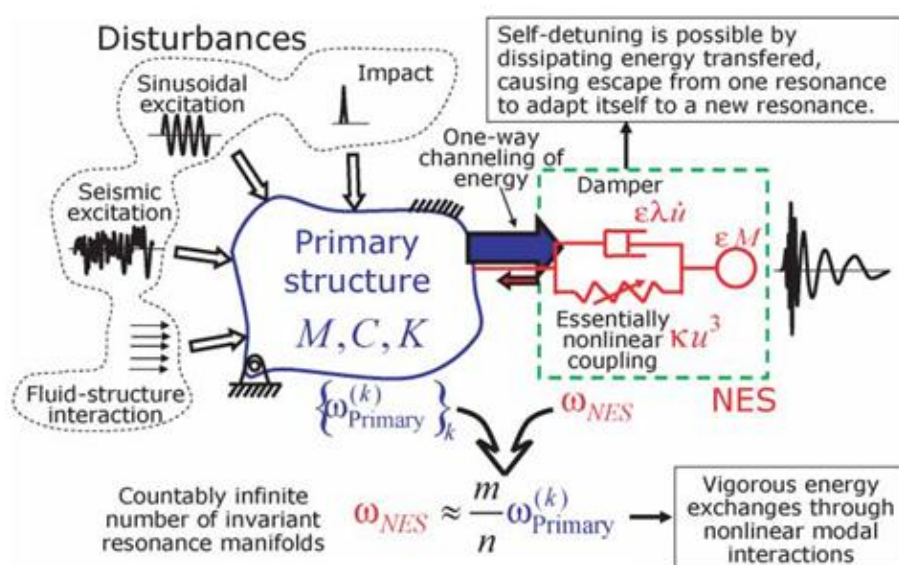


Figure 2.1 Nonlinear resonance (VAKAKIS et al., 2008)

One of the major advantages of this attachment is that it offers nonlinear energy pumping (or targeted energy transfer) under certain conditions. This phenomenon, first reported by Gendelman and his co-authors (GENDELMAN, 2001; GENDELMAN et al., 2001; VAKAKIS; GENDELMAN, 2001), leads to one-way transfer of the vibrational energy from a host structure to the NES, where this energy is localized and dissipated. Although the focus of this work is the piezoelectric NES, several mechanical versions of the device had been proposed. The mass-spring-damper NES with an essentially nonlinear spring was used to study the energy pumping and the influence of the uncertain parameters (the nonlinear stiffness, the NES damping and the host structure damping) in the robustness of the system, identifying limitation for the energy pumping (CATALDO; BELLIZZI; SAMPAIO, 2013). Al-Shudeifat and his co-author presented a numerical and experimental study of a rotating NES (AL-SHUDEIFAT et

al., 2017), displayed in Figure 2.2. The rotating NES was able to passively transfer a significant amount of energy from the low frequency mode of the host structure to the higher frequency one, in which energy is dissipated more effectively.

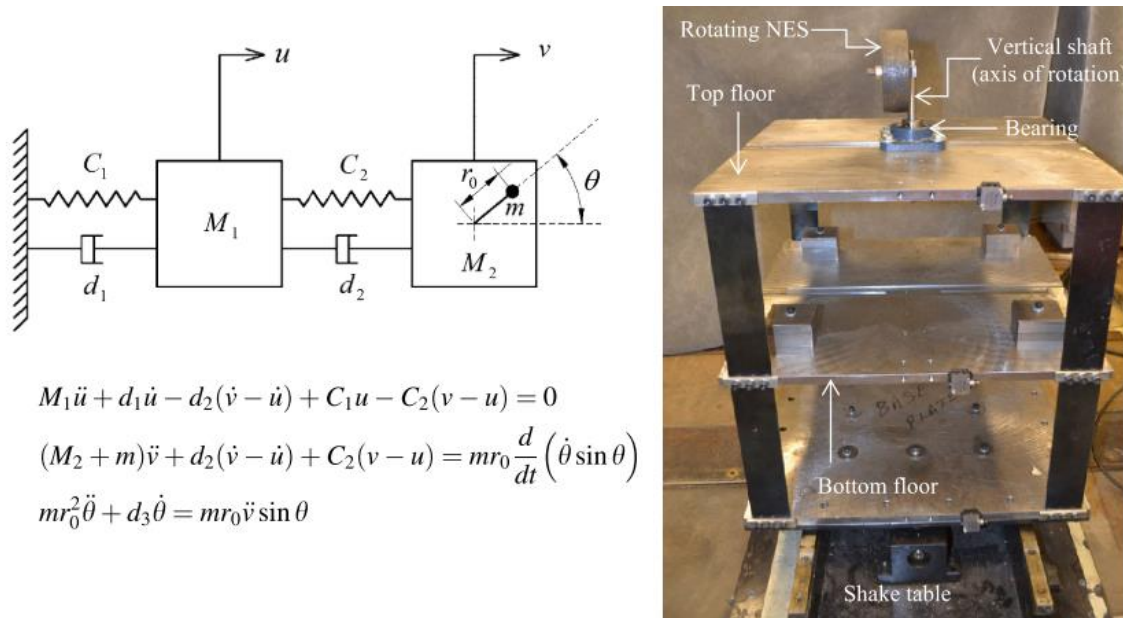


Figure 2.2 Model and experimental setup of the proposed rotating NES (AL-SHUDEIFAT et al., 2017)

MCFARLAND, BERGMAN and VAKAKIS (2005) combined a series of mass, dampers and leaf springs to obtain another mechanical NES. The same configuration was employed on the study of LEE et al. (2005), that investigated in details the triggering mechanisms of limit cycle oscillations in aeroelastic systems, to show that a mechanical NES can be used to eliminate most of the triggering mechanisms. The study was followed by a numerical and an experimental work (LEE et al., 2007a, 2007b), in which an investigation to suppress aeroelastic instabilities of a nonlinear typical section using a single-degree-of-freedom mechanical nonlinear energy sink was presented. They identified three main mechanisms for suppressing aeroelastic instability and presented a complete study of these mechanisms. Exploring these mechanisms, they were able to design a device that provided robust aeroelastic instability suppression even with variation of system parameters. Figure 2.3 and Figure 2.4 display the model of the system (aeroelastic typical section and mechanical NES) and the physical NES used in the experimental setup. The theoretical observations were verified in the experimental paper.



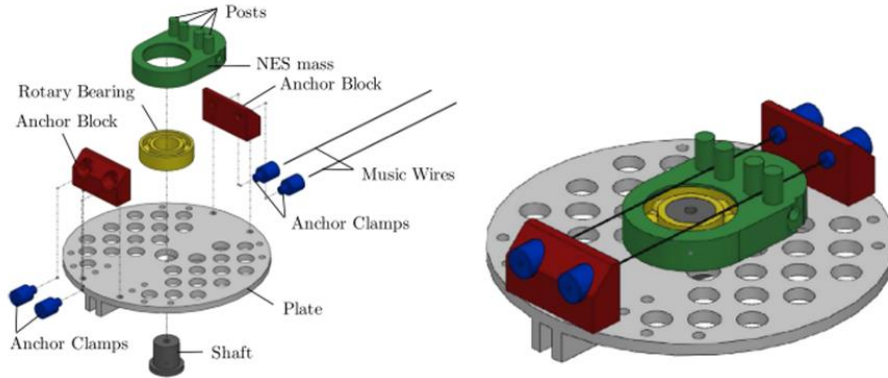


Figure 2.5 Rotating NES (HUBBARD et al., 2010)

Despite the results of the mechanical NES, it is usually a complex mechanical system that requires many different parts and elements to achieve exclusively cubic nonlinearity. In this context, VIGUIÉ, KERSCHEN and RUZZENE (2009) presented the first numerical investigation of a piezoelectric based energy sink with preliminary experimental investigation. The nonlinear shunt presented is displayed in Figure 2.6 and the authors conclude that the influence of the linear inherent capacitance of the piezoelectric should be deeper investigated and they suggests the use of a negative capacitance to overcome this issue.

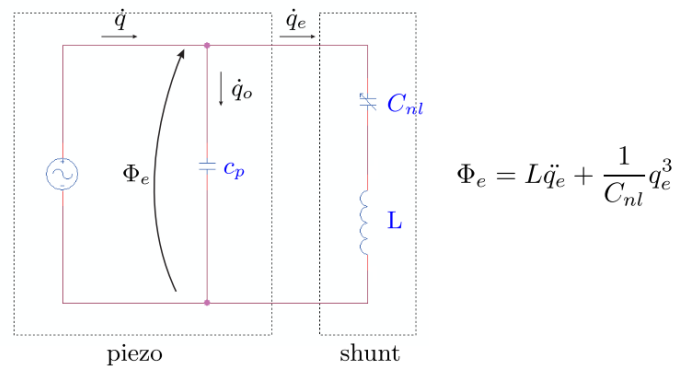


Figure 2.6 Nonlinear shunt (VIGUIÉ; KERSCHEN; RUZZENE, 2009)

More recently, ZHOU, THOUVEREZ and LENOIR (2014) presented the numerical evaluation of an essentially nonlinear shunt circuit for the realization of a piezoelectric NES applied to mistuned bladed disks. The circuit proposed, displayed Figure 2.7 with the model and equations, includes a negative capacitance circuit and the nonlinearity is introduced using a ferroelectric capacitor. Although the voltage-charge behavior of such capacitor is only close to a third degree polynomial, the piezoelectric-

based NES was able to significantly alter the global dynamics of the system, presenting targeted energy transfer from the host structure to the NES under certain conditions.

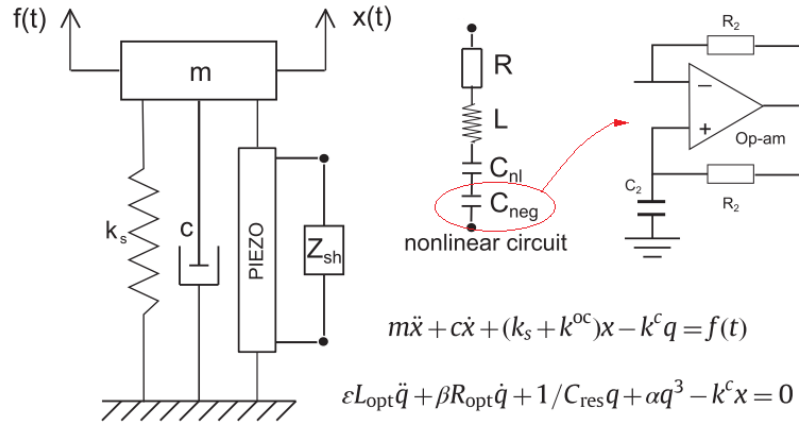


Figure 2.7 Single degree of freedom system of a mass and a piezoelectric element (ZHOU; THOUVEREZ; LENOIR, 2014)

Although relevant numerical analyses and discussions have been presented (VIGUIÉ; KERSCHEN; RUZZENE, 2009; ZHOU; THOUVEREZ; LENOIR, 2014), a nonlinear circuit that allows practical implementation of a piezoelectric NES has only been recently presented, as can be observed in a recent publication from our research group (SILVA; CLEMENTINO; DE MARQUI, 2018).

Although, nonlinearities are easier obtained in the electrical domain of the problem, eliminating complexities of mechanical nonlinear absorbers, using equivalent circuit models can be interesting to represent electromechanical systems in order to better represent the electrical domain. Equivalent circuit models had been presented for single or multiple-degree-of-freedom (SDOF or MDOF), linear and nonlinear piezoelectric coupled systems, in most cases for energy harvesting purposes. ELVIN and ELVIN (2009a) presented an equivalent electrical representation of SDOF and MDOF linear electromechanically coupled systems. The method consists of formulating the system equations of motion using Rayleigh–Ritz approach, decoupling the equations by solving the standard eigenvalue problem and obtaining the electrical equivalent terms so that the coupling terms are represented by ideal transformers. This method is restricted to proportional damping and its accuracy is dependent on the assumed mode shapes, and the number of assumed modes. In another paper (ELVIN; ELVIN, 2009b), the same authors described an explicit coupled finite element – SPICE model. Although the method was used to solve two example problems successfully, the coupling between

the FEM and SPICE models is done explicitly at the end of each time step making the solution computationally expensive. Later, an equivalent circuit for a piezo-patch energy harvester on a thin plate with AC-DC conversion was presented (BAYIK et al., 2016). Until then, the equivalent circuit representations were based on the modal decomposition of the DOFs of the electromechanically coupled system and, then they were limited to mechanically linear systems with linear coupling. To overcome this limitation, two approaches were presented by ELVIN (2014): a system-level circuits approach, which is employed to model the harvester behavior, and a dependent voltage equivalent circuits approach, which are employed to represent the nonlinear system. In this work, equivalent electrical models for linear and nonlinear typical sections are obtained using the dependent voltage approach presented by ELVIN (2014).

### 3 Typical Section Equivalent Electrical Model

Typical section models are commonly used to investigate aeroelastic phenomena such as flutter due to their simplicity and the fundamental insight they provide. This work considers a 2-DOF typical section, which can undergo plunge and pitch displacements. Piezoelectric coupling is added to the plunge DOF of the typical section and the resultant of the electrodes is connected to a nonlinear shunt circuit. This section presents the derivation of the governing equations of the electromechanically coupled system investigated. The unsteady aerodynamic model is also presented. Later, the equivalent electrical model is discussed in detail.

#### 3.1 Typical Section Equations of Motion

The 2-DOF typical section is displayed in Figure 3.1, where  $h$  is the plunge displacement measured at the elastic axis (positive in the downward direction),  $\alpha$  is the pitch angle measured about the elastic axis (positive in the clockwise direction),  $U$  is the airflow speed,  $b$  is the semichord,  $ab$  is the distance from the axis of rotation to the mid-chord,  $x_{ab}$  is the distance of the axis of rotation from the center of gravity,  $K_h$  is the stiffness per length for the plunge DOF,  $K_\alpha$  is the stiffness per length for the pitch DOF,  $M$  is the aerodynamic moment per length,  $F$  is the aerodynamic lift per length and  $V_p$  is the voltage across the piezoelectric electrodes. The damping coefficient per length for the plunge DOF,  $B_h$ , and the damping coefficient per length for the pitch DOF,  $B_\alpha$ , are considered, but are not represented in Figure 3.1.

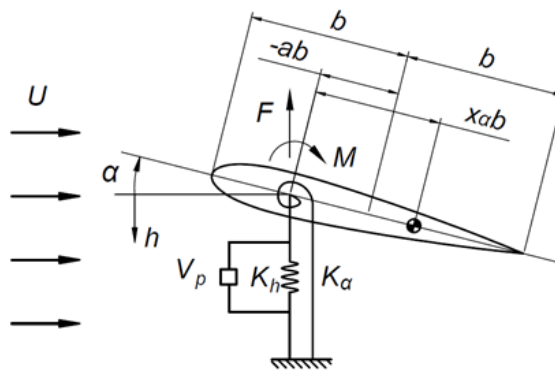


Figure 3.1 Aeroelastic typical section model

The equations of motion of the aeroelastic typical section with electromechanical coupling considered in the plunge DOF are derived by using Lagrange's Method:

$$\begin{cases} \frac{d}{dt} \left( \frac{\partial K}{\partial \dot{h}} \right) - \frac{\partial K}{\partial h} + \frac{\partial P}{\partial h} - \frac{\partial E}{\partial h} = -F - \frac{\partial Q}{\partial \dot{h}} \\ \frac{d}{dt} \left( \frac{\partial K}{\partial \dot{\alpha}} \right) - \frac{\partial K}{\partial \alpha} + \frac{\partial P}{\partial \alpha} - \frac{\partial E}{\partial \alpha} = M - \frac{\partial Q}{\partial \dot{\alpha}} \\ \frac{d}{dt} \left( \frac{\partial K}{\partial \dot{V}_p} \right) - \frac{\partial K}{\partial V_p} + \frac{\partial P}{\partial V_p} - \frac{\partial E}{\partial V_p} = q_p - \frac{\partial Q}{\partial \dot{V}_p} \end{cases} \quad (3.1)$$

where  $K$  is kinetic energy per length,  $P$  is the potential energy per length,  $E$  is the electrical energy per length and  $Q$  is the dissipation function per length. The kinetic energy component can be obtained as:

$$K = \frac{1}{2} m \dot{y}_{CG}^2 + \frac{1}{2} m \dot{x}_{CG}^2 + \frac{1}{2} m_f \dot{h}^2 + \frac{1}{2} I_{CG} \dot{\alpha}^2, \quad (3.2)$$

where  $m$  is the airfoil mass per length,  $m_f$  is the fixture mass per length connecting the airfoil to the plunge springs in the experiments (in the ideal representation,  $m_f = 0$ ),  $I_{CG}$  is the moment of inertia per length about the center of gravity and  $y_{CG}$  and  $x_{CG}$  are respectively the vertical and horizontal coordinates of the center of gravity. Writing the coordinates of the center of gravity in terms of the pitch and plunge coordinates

$$y_{CG} = h + x_\alpha b \sin \alpha \quad (3.3)$$

$$x_{CG} = x_\alpha b (\cos \alpha - 1) \quad (3.4)$$

and integrating over time:

$$\dot{y}_{CG} = \dot{h} + x_\alpha b \dot{\alpha} \cos \alpha \quad (3.5)$$

$$\dot{x}_{CG} = -x_\alpha b \dot{\alpha} \sin \alpha, \quad (3.6)$$

the kinetic energy per length becomes:

$$K = \frac{1}{2} m (\dot{h} + x_\alpha b \dot{\alpha} \cos \alpha)^2 + \frac{1}{2} m (-x_\alpha b \dot{\alpha} \sin \alpha)^2 + \frac{1}{2} m_f \dot{h}^2 + \frac{1}{2} I_{CG} \dot{\alpha}^2 \quad (3.7)$$

$$K = \frac{1}{2} (m + m_f) \dot{h}^2 + \frac{1}{2} [I_{CG} + (x_\alpha b)^2] \dot{\alpha}^2 + m x_\alpha b \dot{h} \dot{\alpha} \cos \alpha. \quad (3.8)$$

Using parallel axis theorem to obtain the moment of inertia per length about the elastic axis ( $I_\alpha$ ) and small-angle approximation

$$K = \frac{1}{2}(m + m_f)\dot{h}^2 + \frac{1}{2}I_\alpha\dot{\alpha}^2 + mx_\alpha b\dot{\alpha}\dot{h}. \quad (3.9)$$

The potential energy per length  $P$ , the electrical energy per length  $E$  and the dissipation function per length  $Q$  are given by:

$$P = \frac{1}{2}K_h h^2 + \frac{1}{2}K_\alpha \alpha^2 - \frac{1}{2} \frac{\theta}{l} h V_p \quad (3.10)$$

$$E = \frac{1}{2}C_p V_p^2 + \frac{1}{2} \frac{\theta}{l} h V_p \quad (3.11)$$

$$Q = \frac{1}{2}B_h \dot{h}^2 + \frac{1}{2}B_\alpha \dot{\alpha}^2 \quad (3.12)$$

where  $l$  is the span length,  $C_p$  is the inherent capacitance of the piezoelectric material,  $\theta$  is the electromechanical coupling term and  $q_p$  is the electrical charge in the piezoelectric material. Applying Lagrange's equations (3.1), the typical section governing equations considering the fixture mass connecting the airfoil to the plunge springs in the experiments are obtained as:

$$\begin{cases} (m + m_f)\ddot{h} + S_\alpha \ddot{\alpha} + B_h \dot{h} + K_h h - \frac{\theta}{l} V_p = -F \\ S_\alpha \ddot{h} + I_\alpha \ddot{\alpha} + B_\alpha \dot{\alpha} + K_\alpha \alpha = M \\ C_p \dot{V}_p + \dot{q}_p + \theta \dot{h} = 0 \end{cases} \quad (3.13)$$

where  $S_\alpha = mx_\alpha b$  is the static moment coupling the degrees of freedom.

### 3.1.1 Nonlinear Typical Section

The typical section presented in the previous section considers linear and concentrated springs and dampers. In this section, a nonlinearity is added to the pitch DOF. This effect adds a term in the piezoaeroelastic equations representing the nonlinear restoring moment  $f_{nl}(\alpha)$ :

$$\begin{cases} (m + m_f)\ddot{h} + S_\alpha \ddot{\alpha} + B_h \dot{h} + K_h h - \frac{\theta}{l} V_p = -F \\ S_\alpha \ddot{h} + I_\alpha \ddot{\alpha} + B_\alpha \dot{\alpha} + K_\alpha \alpha + f_{nl}(\alpha) = M \\ C_p \dot{V}_p + \dot{q}_p + \theta \dot{h} = 0 \end{cases} \quad (3.14)$$

In this work, a concentrated nonlinearity, free play, is considered. The free play or bilinear stiffness is used to represent a clearance in the airfoil fixture. The restoring moment for the free play in the pitch DOF,  $f_{fp}(\alpha)$ , is given by:

$$f_{fp}(\alpha) = \begin{cases} -K_{\alpha}\alpha_{fp} & \alpha > \alpha_{fp} \\ 0 & -\alpha_{fp} < \alpha < \alpha_{fp} \\ K_{\alpha}\alpha_{fp} & \alpha < -\alpha_{fp} \end{cases} \quad (3.15)$$

where  $\alpha_{fp}$  is the semi free play gap. The restoring moments in the pitch DOF for the linear and the free play are presented in Figure 3.2.

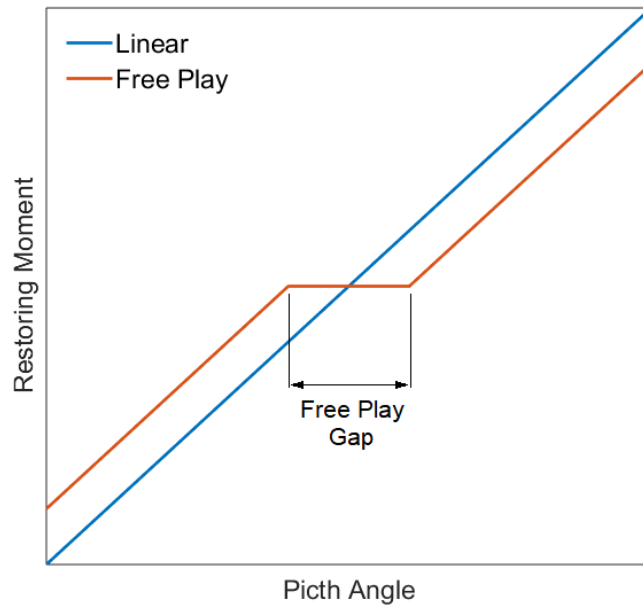


Figure 3.2 Restoring moments in the pitch DOF for the linear and the free play configurations

### 3.1.2 Aerodynamic Loads

The next step is to determine the non-stationary aerodynamic loads. THEODORSEN (1935) considers a thin, symmetric two-dimensional airfoil of semichord  $b$ , with the axis of rotation positioned at distance  $a$  (per semichord) aft of the mid-chord (Figure 3.1). According to thin airfoil theory, the center of pressure and the aerodynamic center of a thin, symmetric airfoil under incompressible flow are coincident and lie on one quarter of the chord behind the leading edge. In this work, the axis of rotation is positioned exactly in this point.

The classical solution for the lift and moment about the flexural axis, both expressed per unit span (BISPLINGHOFF; ASHLEY; HALFMAN, 1996), may be written as:

$$F = \pi\rho b^2(\ddot{h} + U\dot{\alpha} - ba\ddot{\alpha}) + 2\pi\rho UbC(k) \left[ \dot{h} + U\alpha + b\left(\frac{1}{2} - a\right)\dot{\alpha} \right] \quad (3.16)$$

$$M = \pi\rho b^2 \left[ ba\ddot{h} - Ub\left(\frac{1}{2} - a\right)\dot{\alpha} - b^2\left(\frac{1}{8} + a^2\right)\ddot{\alpha} \right] \\ + 2\pi\rho Ub^2 \left( a + \frac{1}{2} \right) C(k) \left[ \dot{h} + U\alpha + b\left(\frac{1}{2} - a\right)\dot{\alpha} \right] \quad (3.17)$$

where  $\rho$  is the density of the fluid,  $C(k)$  is the Theodorsen's function and  $k = \omega b/U$  is the reduced frequency, which is a dimensionless parameter that indicates how unsteady the system is.

The first term of each expression shows the noncirculatory terms, which are an "apparent inertia" (these terms are of minor importance for bending/torsion type flutter of cantilever wings at low reduced frequencies but are more important for flutter of control surfaces at higher reduced frequencies). The second part shows the circulatory terms, or forces whose creation is related to vorticity in the flow and are dependent upon the value of Theodorsen's function. Theodorsen's function attenuates the aerodynamic loads depending on the frequency of oscillation and can only be applied in case of harmonic motion.

Considering harmonic motion,  $h = h_0 e^{i\omega t}$  and  $\alpha = \alpha_0 e^{i\omega t}$  and using the complex form of Theodorsen's function,  $C(k) = C_{Re}(k) + iC_{Im}(k)$ , the aerodynamic loads can be rewritten as:

$$F = \rho U^2 b \left\{ \left[ -2\pi \left( \frac{k^2}{2} + kC_{Im} \right) + ik2\pi C_{Re} \right] \frac{h_0}{b} \right. \\ + \left[ 2\pi \left( \frac{k^2 a}{2} + C_{Re} - kC_{Im} \left( \frac{1}{2} - a \right) \right) \right. \\ \left. \left. + ik2\pi \left( \frac{1}{2} + \frac{C_{Im}}{k} + C_{Re} \left( \frac{1}{2} - a \right) \right) \right] \alpha_0 \right\} e^{i\omega t} \quad (3.18)$$

$$\begin{aligned}
M = \rho U^2 b^2 \left\{ \left[ -2\pi \left( \frac{k^2 a}{2} + k C_{Im} \left( a + \frac{1}{2} \right) \right) + ik 2\pi C_{Re} \left( a + \frac{1}{2} \right) \right] \frac{h_0}{b} \right. \\
+ \left[ 2\pi \left( \frac{k^2}{2} \left( \frac{1}{8} + a^2 \right) + C_{Re} \left( a + \frac{1}{2} \right) \right. \right. \\
- \left. \left. k C_{Im} \left( a + \frac{1}{2} \right) \left( \frac{1}{2} - a \right) \right) \right. \\
+ \left. ik 2\pi \left( -\frac{1}{2} \left( \frac{1}{2} - a \right) + \frac{C_{Im}}{k} \left( a + \frac{1}{2} \right) \right) \right. \\
\left. \left. + C_{Re} \left( a + \frac{1}{2} \right) \left( \frac{1}{2} - a \right) \right) \right] \alpha_0 \right\} e^{i\omega t}
\end{aligned} \tag{3.19}$$

or, in the oscillatory derivative form:

$$F = \rho U^2 b \left\{ (F_h + ik F_{\dot{h}}) \frac{h_0}{b} + (F_\alpha + ik F_{\dot{\alpha}}) \alpha_0 \right\} e^{i\omega t} \tag{3.20}$$

$$M = \rho U^2 b^2 \left\{ (M_h + ik M_{\dot{h}}) \frac{h_0}{b} + (M_\alpha + ik M_{\dot{\alpha}}) \alpha_0 \right\} e^{i\omega t} \tag{3.21}$$

where  $F_h$ ,  $F_{\dot{h}}$ ,  $F_\alpha$ ,  $F_{\dot{\alpha}}$ ,  $M_h$ ,  $M_{\dot{h}}$ ,  $M_\alpha$  and  $M_{\dot{\alpha}}$  are the nondimensional oscillatory aerodynamic derivatives. These derivatives are expressed in terms of the normalized displacement for plunge and pitch. Comparing Equation (3.18) to (3.20) and Equation (3.19) to (3.21), the derivatives can be written as:

$$\begin{aligned}
F_h &= -2\pi \left( \frac{k^2}{2} + k C_{Im} \right) \\
F_{\dot{h}} &= 2\pi C_{Re} \\
F_\alpha &= 2\pi \left[ \frac{k^2 a}{2} + C_{Re} - k C_{Im} \left( \frac{1}{2} - a \right) \right] \\
F_{\dot{\alpha}} &= 2\pi \left[ \frac{1}{2} + C_{Re} \left( \frac{1}{2} - a \right) + \frac{C_{Im}}{k} \right] \\
M_h &= -2\pi \left( \frac{k^2 a}{2} + k C_{Im} \left( a + \frac{1}{2} \right) \right) \\
M_{\dot{h}} &= 2\pi C_{Re} \left( a + \frac{1}{2} \right) \\
M_\alpha &= 2\pi \left[ \frac{k^2}{2} \left( \frac{1}{8} + a^2 \right) + C_{Re} \left( a + \frac{1}{2} \right) - k C_{Im} \left( a + \frac{1}{2} \right) \left( \frac{1}{2} - a \right) \right] \\
M_{\dot{\alpha}} &= 2\pi \left[ -\frac{1}{2} \left( \frac{1}{2} - a \right) + C_{Re} \left( a + \frac{1}{2} \right) \left( \frac{1}{2} - a \right) + \frac{C_{Im}}{k} \left( a + \frac{1}{2} \right) \right]
\end{aligned} \tag{3.22}$$

Substituting the harmonic motion solution and the reduced frequency in Equations (3.20) and (3.21) the aerodynamic loads can be written as:

$$F = \rho U^2 F_h h + \rho U b F_{\dot{h}} \dot{h} + \rho U^2 b F_{\alpha} \alpha + \rho U b^2 F_{\dot{\alpha}} \dot{\alpha} \quad (3.23)$$

$$M = \rho U^2 b M_h h + \rho U b^2 M_{\dot{h}} \dot{h} + \rho U^2 b^2 M_{\alpha} \alpha + \rho U b^3 M_{\dot{\alpha}} \dot{\alpha} \quad (3.24)$$

that can be substituted in Equation (3.13):

$$\begin{cases} (m + m_f) \ddot{h} + (B_h + \rho U b^2 F_{\dot{h}}) \dot{h} + (K_h + \rho U^2 b F_h) h + S_{\alpha} \ddot{\alpha} + (\rho U b^2 F_{\dot{\alpha}}) \dot{\alpha} + (\rho U^2 b F_{\alpha}) \alpha - \frac{\theta}{l} v_p = 0 \\ I_{\alpha} \ddot{\alpha} + (B_{\alpha} - \rho U b^3 M_{\dot{\alpha}}) \dot{\alpha} + (K_{\alpha} - \rho U^2 b^2 M_{\alpha}) \alpha + S_{\alpha} \dot{h} + (-\rho U b^3 M_{\dot{h}}) \dot{h} + (-\rho U^2 b^2 M_h) h = 0 \\ C_p \dot{v}_p + \dot{q}_p + \theta \dot{h} = 0 \end{cases} \quad (3.25)$$

It is important to observe that the aerodynamic loads can be written in terms of structural displacement and velocity and their effects on the aeroelastic behavior of the system are represented as modified structural stiffness and damping due to unsteady aerodynamics, which allows the flutter aeroelastic instability.

### 3.2 Equivalent Electrical Model

When dealing with electromechanically coupled systems, it is convenient to model them with electrical equivalent circuits, so that the entire system is represented in the electrical domain. The equivalent electrical model of the typical section developed by ELVIN (2014) is presented in Figure 3.3, where the piezoelectric material is represented by a current source in series with its inherent capacitance (Norton representation). Another representation for the piezoelectric material is a voltage source in parallel with the capacitance (Thevenin representation), which could also be applied without significant changes.

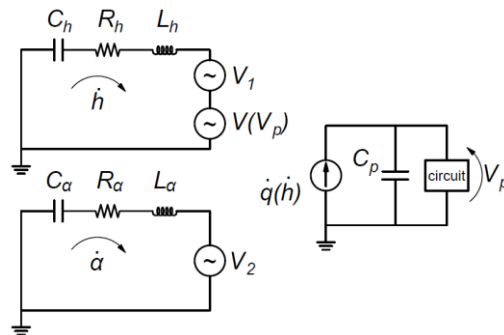


Figure 3.3 Equivalent electrical circuit for a 2-DOF aeroelastic typical section  
Adapted from ELVIN (2014)

In order to obtain the electrical circuit, each mechanical term is replaced by its electrical analog (inertial terms are replaced by inductors  $L$ , damping terms by resistor  $R$  and stiffness terms by the inverse of capacitors  $C$ ). The mechanical equation (3.25) becomes:

$$\begin{cases} L_h \ddot{h} + R_h \dot{h} + \frac{1}{C_h} h + S_\alpha \ddot{\alpha} + c_2 \dot{\alpha} + c_3 \alpha - \frac{\theta}{l} V_p = 0 \\ L_\alpha \ddot{\alpha} + R_\alpha \dot{\alpha} + \frac{1}{C_\alpha} \alpha + S_\alpha \ddot{h} + c_5 \dot{h} + c_6 h = 0 \\ C_p \dot{V}_p + \dot{q}_p + \theta \dot{h} = 0 \end{cases} \quad (3.26)$$

where the electrical elements are obtained as in Table 1.

Plunge circuit		Pitch circuit	
Electrical Elements	Elastic/ Aeroelastic	Electrical Elements	Elastic/ Aeroelastic
$L_h$	$(m + m_f)$	$L_\alpha$	$I_\alpha$
$R_h$	$(B_h + \rho U b^2 F_{\dot{h}})$	$R_\alpha$	$(B_\alpha - \rho U b^3 M_{\dot{\alpha}})$
$C_h$	$\frac{1}{(K_h + \rho U^2 b F_h)}$	$C_\alpha$	$\frac{1}{(K_\alpha - \rho U^2 b^2 M_\alpha)}$
$c_2$	$\rho U b^2 F_{\dot{\alpha}}$	$c_5$	$-\rho U b^3 M_{\dot{h}}$
$c_3$	$\rho U^2 b F_\alpha$	$c_6$	$-\rho U^2 b^2 M_h$

The circuit of Figure 3.3 uses two voltage-controlled voltage sources ( $V_1$  and  $V_2$ ) to provide the DOFs coupling. The first voltage source  $V_1$  is obtained from the plunge equation and the second voltage source  $V_2$  is obtained from the pitch equation.

$$V_1 = S_\alpha \ddot{\alpha} + c_2 \dot{\alpha} + c_3 \alpha \quad (3.27)$$

$$V_2 = S_\alpha \ddot{h} + c_5 \dot{h} + c_6 h \quad (3.28)$$

In the plunge circuit, the electromechanical coupling is represented by another voltage-controlled voltage source  $V(V_p)$ . In the piezoelectric material circuit, the electromechanical coupling is represented by a current-controlled source  $\dot{q}(\dot{h})$  adding a current corresponding to the direct piezoelectric effect.

$$V(V_p) = -\frac{\theta}{l} V_p \quad (3.29)$$

$$\dot{q}(\dot{h}) = \theta \dot{h} \quad (3.30)$$

In the simulations, the dependent sources are represented by the following elements of MatLab:

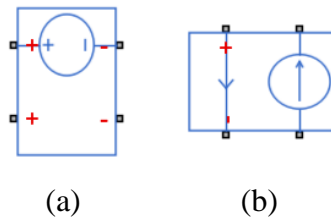


Figure 3.4 Voltage-controlled (a) and current-controlled (b) voltage source from MatLab Simulink

It means each term of Equations (3.27), (3.28), (3.29) and (3.30) is represented by a single source  $CS_n$  or:

$$\begin{aligned} V_1 &= CS_1 + CS_2 + CS_3 \\ V_2 &= CS_4 + CS_5 + CS_6 \\ V(V_p) &= CS_7 \\ \dot{q}(\dot{h}) &= CS_8 \end{aligned} \quad (3.31)$$

To calculate the controlled sources, it is necessary to obtain the displacements, velocities and accelerations, by measuring its electrical analogs directly in the electrical circuit. The controlled sources  $CS_n$  can be calculated according Table 2.

Table 2. Electrical sources

Source	Relation	Source	Relation
$CS_1$	$S_\alpha \ddot{\alpha} = \frac{S_\alpha}{L_\alpha} V(L_\alpha)$	$CS_5$	$c_5 \dot{h} = \frac{c_5}{R_h} V(R_h)$
$CS_2$	$c_2 \dot{\alpha} = \frac{c_2}{R_\alpha} V(R_\alpha)$	$CS_6$	$c_6 h = \frac{c_6}{1/C_h} V(C_h)$
$CS_3$	$c_3 \alpha = \frac{c_3}{1/C_\alpha} V(C_\alpha)$	$CS_7$	$-\frac{\theta}{l} V_p = -\frac{\theta}{l} V(C_p)$
$CS_4$	$S_\alpha \ddot{h} = \frac{S_\alpha}{L_h} V(L_h)$	$CS_8$	$\theta \dot{h} = \theta i(R_h)$

The resultant circuit is displayed in Figure 3.5, which already includes the NES in the “circuit” block of Figure 3.3.

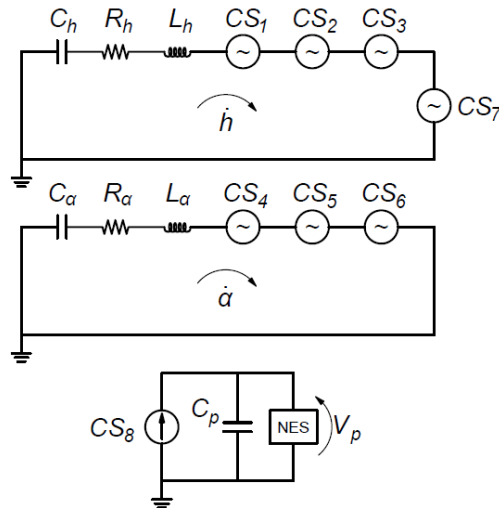


Figure 3.5 Equivalent electrical circuit for a 2-DOF aeroelastic typical section with NES

### 3.2.1 Nonlinear Equivalent Electrical Model

In order to represent the free play in the pitch degree of freedom, the pitch circuit is replaced by:

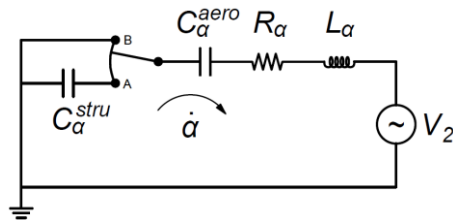


Figure 3.6 Pitch equivalent electrical circuit with free play

In the equivalent circuit of Figure 3.6, the pitch capacitor  $C_\alpha$  is split in two to represent the mechanical ( $C_\alpha^{stru}$ ) and the aeroelastic ( $C_\alpha^{aero}$ ) contributions independently. Besides, a switch is added so that the capacitance relative to the mechanical stiffness is short-circuited when the pitch angle is inside the free play gap. As a result, the pitch mechanical stiffness is only activated outside the free play gap.

## 4 Nonlinear Energy Sink

This chapter introduces the concept of nonlinear energy sinks as well as the basic equations for the piezoelectric case. Moreover, the nonlinear shunt circuit developed and employed in the simulations and experiments is also presented. The mechanical concept of a nonlinear energy sink is displayed in Figure 4.1 applied to the plunge DOF of the typical section

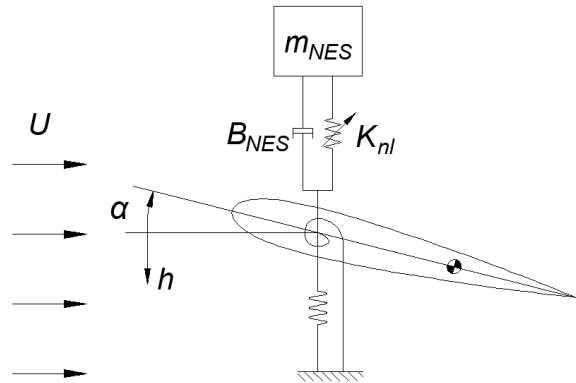


Figure 4.1 Mechanical NES applied to the plunge DOF of the typical section

where  $m_{NES}$  is the mass of the nonlinear vibration absorber,  $B_{NES}$  is the damping and  $K_{nl}$  is the stiffness, which is exclusively cubic. The equation of the free mechanical NES is:

$$m_{NES}\ddot{h} + B_{NES}\dot{h} + K_{nl}h^3 = 0. \quad (4.1)$$

For the electrical realization of the NES, the mechanical terms are replaced by its electrical analog. Therefore, the NES circuit can be obtained from a linear resonant circuit, RL, in series with a nonlinear capacitance,  $C_{nl}$ . Another difference between mechanical and electrical NES is that the coupling between the typical section (mechanical domain) and the absorber (electrical domain) is through the piezoelectric material. Since the internal capacitance of piezoelectric material would avoid the realization of essential nonlinearity, which is required for a NES, a negative capacitance ( $C_{neg} < 0$ ) is also connected in series to minimize the linear stiffness of the system (ZHOU; THOUVEREZ; LENOIR, 2014), leading to the nonlinear circuit shown in Figure 4.2.

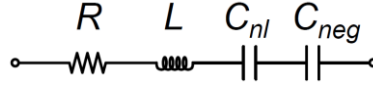


Figure 4.2 Electrical NES

When the piezoelectric material is connected to the NES circuit, the electrical equation of the system becomes:

$$L\ddot{q}_p + R\dot{q}_p + \beta q_p^3 + \frac{1}{C_{neg}} q_p + \left( \frac{1}{C_p} q_p + \frac{\theta}{C_p} h \right) = 0 \quad (4.2)$$

where the first three terms are the electrical equivalent of equation (4.1), the fourth term is due to the negative capacitance and the terms in parenthesis are the voltage across the piezoelectric material. In addition,  $\beta$  is the coefficient of the cubic term (related to the nonlinear capacitance,  $C_{nl}$ ). Defining the residual capacitance as the linear remaining capacitance related to the negative capacitance and the capacitance of the piezoelectric material:

$$\frac{1}{C_{res}} = \frac{1}{C_{neg}} + \frac{1}{C_p}, \quad (4.3)$$

and rearranging the terms, the electrical equation of (3.25) becomes:

$$L\ddot{q}_p + R\dot{q}_p + \frac{1}{C_{res}} q_p + \beta q_p^3 + \frac{\theta}{C_p} h = 0. \quad (4.4)$$

#### 4.1 Proposed Nonlinear Energy Sink Circuit

The circuit configuration of Figure 4.2 introduces nonlinearity to the system through a nonlinear capacitance ( $C_{nl}$ ). ZHOU, THOUVEREZ and LENOIR (2014) suggest the use of ferroelectric capacitors to introduce nonlinearity to the electromechanical system. As the nonlinear voltage-charge characteristic of ferroelectric capacitors is usually only close to a third-degree polynomial and the linear term hinders the realization of essential nonlinearity, in this work it is replaced by a nonlinear capacitance circuit. Therefore, a negative capacitance ( $C_{neg}$ ) in series with both the nonlinear capacitor and the internal capacitance of piezoelectric material enables minimization (ideally elimination) of the linear voltage-charge behavior.  $C_{neg}$  and  $C_{nl}$  are obtained synthetically as shown in Figure 4.3 (SILVA; CLEMENTINO; DE MARQUI, 2018). The red highlight indicates the negative capacitance circuit and the

blue one indicates the nonlinear capacitance circuit, and both will be discussed in detail along this section.

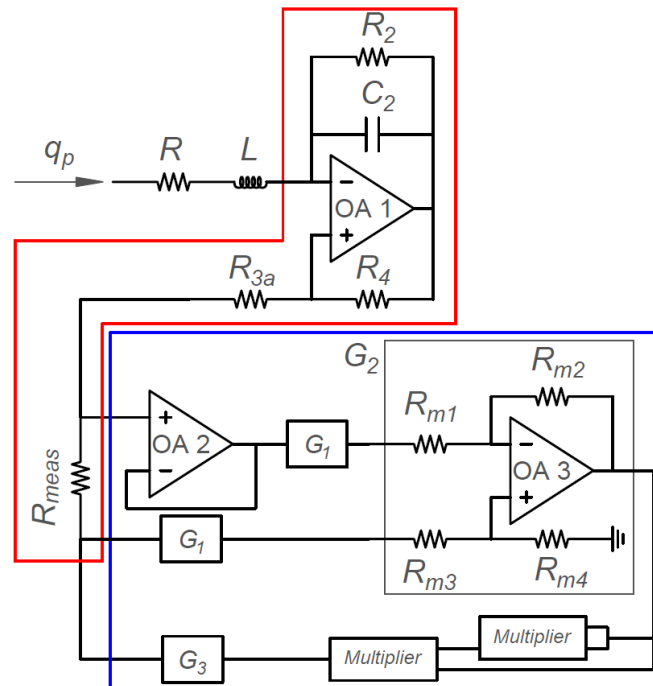


Figure 4.3 Nonlinear energy sink circuit with negative capacitance (red) and cubic nonlinearity (blue)

Although the circuit shown in Figure 4.3 uses operational amplifiers (OA) that requires external power source it does not actuate to suppress oscillations and, therefore can be considered a passive control technique as well as the mechanical NES and the theory of the piezoelectric based NES.

For the negative capacitance, this work uses the circuit presented in literature (BECK; CUNEFARE; COLLET, 2013; BEHRENS; FLEMING; MOHEIMANI, 2001), which is shown in Figure 4.4.

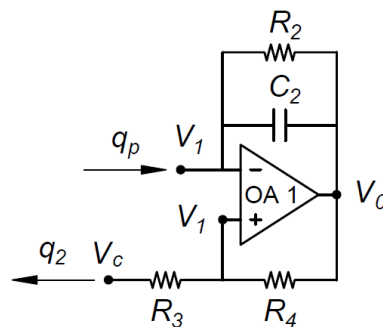


Figure 4.4 Negative capacitance circuit schematic

As demonstrated by BECK, CUNEFARE and COLLET (2013), the resistor  $R_2$  in Figure 4.4 is required to stabilize the OA 1 but is large enough so that the current across it can be considered negligible. Applying Kirchhoff's voltage law:

$$V_1 - \frac{1}{C_2}q_p - (R_3 + R_4)\dot{q}_2 = V_c \quad (4.5)$$

$$V_1 - R_3\dot{q}_2 = V_c \quad (4.6)$$

it is possible to obtain the negative capacitance relation:

$$V_1 - V_c = -\frac{1}{C_2} \frac{R_3}{R_4} q_p \quad (4.7)$$

$$C_{neg} = -\frac{R_4}{R_3} C_2 \quad (4.8)$$

and the relation between the electric charges:

$$R_3 = \frac{V_1 - V_c}{\dot{q}_2} = \frac{1}{\dot{q}_2} \left( -\frac{1}{C_2} \frac{R_3}{R_4} q_p \right) \quad (4.9)$$

$$\dot{q}_2 = -\frac{1}{R_4 C_2} q_p = -\frac{1}{R_4 C_2} C_p v_p \quad (4.10)$$

To adjust the nonlinear voltage ( $V_c = \beta q_p^3$ ), resistance  $R_3$  is split in  $R_{3a}$  and  $R_{meas}$ . The resultant circuit is shown in Figure 4.5.

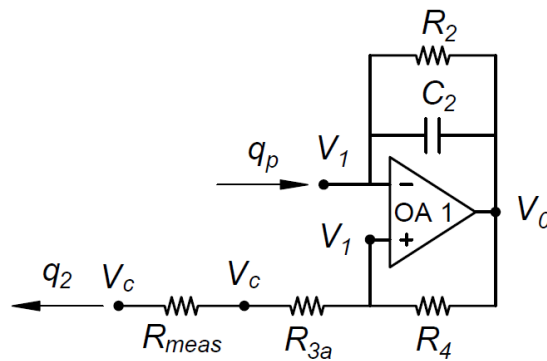


Figure 4.5 Negative capacitance circuit

A voltage buffer amplifier (OA 2) copies the intermediate voltage  $V_r$  without interfering in the negative capacitance circuit. The voltage across  $R_{meas}$  can be calculated from:

$$V_c - V_r = -R_{meas}\dot{q}_2 = \frac{R_{meas}C_p v_p}{R_4 C_2} = -\frac{R_{meas}C_p v_p}{R_3 C_{neg}} \quad (4.11)$$

and as  $R_{meas} + R_{3a} = R_3$ , the relation  $\frac{R_{meas}}{R_3}$  belongs to the interval  $[0,1]$  and  $V_r$  belongs to the interval  $\left[V_c, V_c + \frac{C_p v_p}{C_{neg}}\right]$ . For the proper operation of the circuit,  $R_{meas}$  is defined so that the range of voltages  $V_r$  is equivalent to twice the voltage across the operational amplifiers or:

$$V_{rmax} - V_{rmin} \approx 2V_{Op-Ampmax} \quad (4.12)$$

this condition may not be satisfied since  $\frac{R_{meas}}{R_3}$  is restricted. In this case,  $R_{meas}$  is chosen so that the condition is satisfied for as long as possible.

The voltages  $V_r$  and  $V_c$  are adjusted, if necessary. This step uses the same circuit for both voltages, which consists in a voltage divider followed by a voltage buffer amplifier (OA 4), as shown in Figure 4.6.

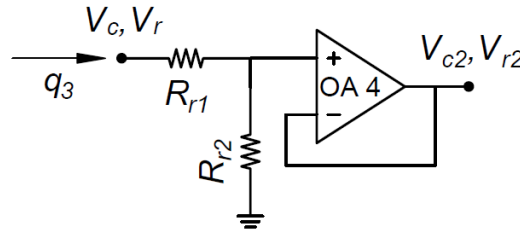


Figure 4.6  $G_1$  circuit

Since  $V_c > V_r$ , the resistors are adjusted according to  $V_c$ . Defining the gain of the circuit:

$$G_1 = \frac{V_{r2}}{V_r} = \frac{V_{c2}}{V_c} \quad (4.13)$$

that is chosen so that  $G_1 = \frac{V_{Op-Ampmax}}{V_{cmax}}$ . If the circuit of Figure 4.6 is applied,

Kirchhoff's voltage law:

$$V_{c,r} - (R_{r1} + R_{r2})\dot{q}_3 = 0 \quad (4.14)$$

$$V_{c,r} - R_{r1}\dot{q}_3 = V_{c2,r2} \quad (4.15)$$

allows to obtain the resistors relation:

$$V_{c2,r2} = \frac{R_{r2}}{(R_{r1} + R_{r2})} V_{c,r} = G_1 V_{c,r} \quad (4.16)$$

$$R_{r2} = \frac{R_{r1} G_1}{(1 - G_1)} \quad (4.17)$$

Despite de adjustment of voltages  $V_r$  and  $V_c$ , the differential amplifier of Figure 4.7 compares both voltages.

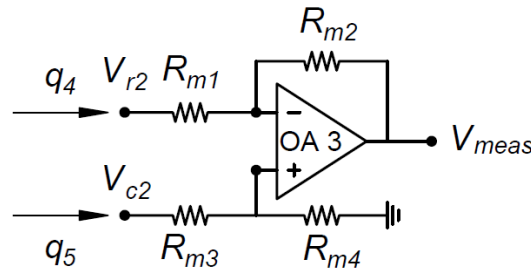


Figure 4.7  $G_2$  circuit (differential amplifier)

Applying Kirchhoff's voltage law:

$$V_{r2} - (R_{m1} + R_{m2})\dot{q}_4 = V_{meas} \quad (4.18)$$

$$V_{c2} - (R_{m3} + R_{m4})\dot{q}_5 = 0 \quad (4.19)$$

$$V_{r2} - R_{m1}\dot{q}_4 - R_{m4}\dot{q}_5 = 0 \quad (4.20)$$

The output voltage is:

$$V_{meas} = -\frac{R_{m2}}{R_{m1}} G_1 V_r + \left( \frac{R_{m1} + R_{m2}}{R_{m1}} \right) \left( \frac{R_{m4}}{R_{m3} + R_{m4}} \right) \left( \frac{R_{m2}}{R_{m1}} G_1 \right) V_c \quad (4.21)$$

The differential amplifier circuit from Figure 4.7 is adjusted so that  $V_{meas}$  and the voltage across  $R_{meas}$  reach their maximum values simultaneously. For that, the gain of the circuit ( $G_2$ ) is obtained as:

$$G_2 = \frac{V_{meas}}{(V_r - V_c)} = \frac{V_{measmax}}{R_{meas}} R_4 C_2 C_p v_{pmax} \quad (4.22)$$

The resistors relation is obtained by making both terms of Equation (4.21) equal to  $G_2$ . From first term:

$$R_{m2} = \frac{R_{m1} G_2}{G_1} \quad (4.23)$$

From second term:

$$\left(\frac{R_{m1}+R_{m2}}{R_{m1}}\right)\left(\frac{R_{m4}}{R_{m3}+R_{m4}}\right)\frac{R_{m2}}{R_{m1}}G_1 = G_2 \quad (4.24)$$

$$\frac{R_{m3} + R_{m4}}{R_{m4}} = \left(1 + \frac{G_2}{\gamma_1}\right)\frac{G_1}{G_2} = \frac{G_1 + G_2}{G_2} \quad (4.25)$$

$$R_{m4} = R_{m3} \frac{\left(\frac{G_1 + G_2}{G_2}\right)}{1 - \left(\frac{G_1 + G_2}{G_2}\right)} \quad (4.26)$$

To obtain the nonlinearity, the amplified output voltage  $V_{meas}$  is driven to the voltage multipliers and divided by 100 (voltage multipliers gain). The output voltage is finally adjusted to be equal to the nonlinear voltage  $V_c$ :

$$V_c = G_3 \frac{V_{meas}^3}{100} = G_3 \frac{G_2^3 (V_c - V_r)^3}{100} = G_3 G_2^3 \frac{(R_{meas} C_p v_p)^3}{100 (R_4 C_2)^3} = \beta q_p^3 \quad (4.27)$$

$$G_3 = \frac{100 \beta (R_4 C_2)^3}{(G_2 R_{meas})^3} \quad (4.28)$$

To obtain gain  $G_3$ , the circuit of Figure 4.8 is used.

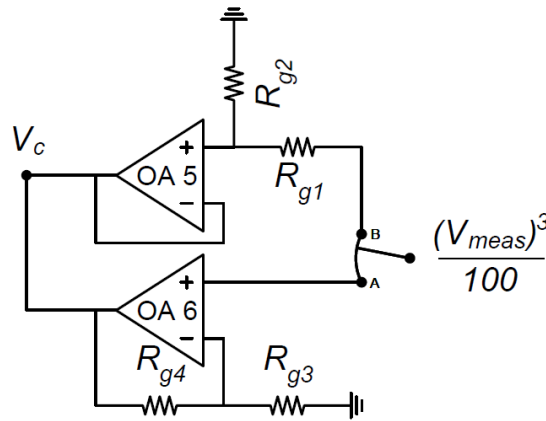


Figure 4.8  $G_3$  circuit

If  $G_3 \geq 1$ , the switch in Figure 4.8 connects to terminal A:

$$V_c = \left(1 + \frac{R_{g4}}{R_{g3}}\right) \frac{V_{meas}^3}{100} = G_3 \frac{V_{meas}^3}{100} \quad (4.29)$$

$$R_{g4} = (G_3 - 1)R_{g3} \quad (4.30)$$

Otherwise, the switch connects to terminal B:

$$V_c = \left( \frac{R_{g2}}{R_{g1} + R_{g2}} \right) \frac{V_{meas}^3}{100} = G_3 \frac{V_{meas}^3}{100} \quad (4.31)$$

$$R_{g2} = \left( \frac{G_3}{1 - G_3} \right) R_{g1} \quad (4.32)$$

As a major advantage, the proposed piezoelectric NES circuit can easily be modified by changing a few electrical components. For example, the nonlinear coefficient of cubic stiffness term  $\beta$  in Equation (4.4) can be modified by changing the resistors of  $G_3$  circuit. It is also important to note that various nonlinear piezoelectric absorbers (and various other nonlinearities, e.g. Duffing-type) can be achieved through simple modifications to the circuit presented in Figure 4.3. Finally, the equivalent model of the coupled typical section presented in section 3.2 can be combined to the NES circuit.

## 5 Effects of Piezoelectric Based NES on the Aeroelastic Behavior of the Linear Typical Section

The NES circuit presented in section 4.1 is connected to the equivalent electric model presented in section 3.2, so that the electromechanically coupled system is fully represented in the electrical domain. Initially in this section, preliminary analysis is performed considering aeroelastic parameters for linear typical section of some previous work developed in our research group. Later, the parameters of the experimental typical section are identified and used in aeroelastic simulations to adjust the nonlinear shunt circuit and verify its effects on the aeroelastic behavior. Experimental verifications are also provided.

### 5.2 Evaluation of Voltage Magnitudes Of The Piezoelectric Material

Preliminary simulations are performed with the NES block diagram, so that the effects of the NES parameters ( $L$ ,  $R$ ,  $C_{res}$  and  $\beta$ ) can be analyzed without calculating the circuit elements. The NES block diagram is displayed in Figure 5.1 (solution of Equation (4.4)) and is combined to the equivalent electrical model of the linear typical section in MATLAB/Simulink. The aeroelastic parameters of the typical section are the same used in previous work developed in our research group (D'ASSUNÇÃO; DE MARQUI, 2015).

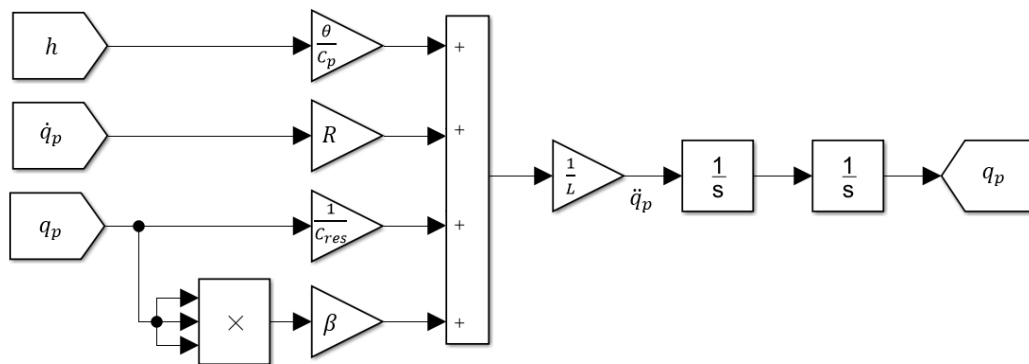


Figure 5.1 NES block diagram

Although the block diagram does not represent the behavior of the circuit perfectly, the results are useful to identify the magnitude of the voltages across the piezoelectric material. Different from the elastic case presented by SILVA et al. (2018), which explores the performance of the piezoelectric NES on a cantilever, the voltage

output from piezoelectric material can reach hundreds of volts and the voltage in the negative capacitance circuit is even higher. Therefore, the operational amplifier in the negative capacitance circuit of Figure 4.5 is replaced by the discrete operational amplifier of Figure 5.2.

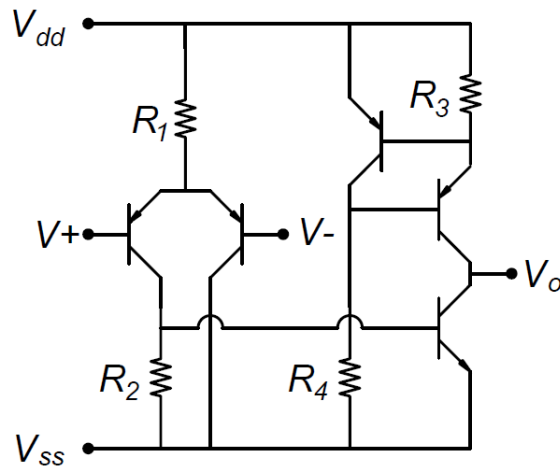


Figure 5.2 Discrete operational amplifier

To adjust the parameters of the high-voltage operational amplifier, the circuit (Figure 5.2) was tested in the configuration of Figure 5.3. Given an input voltage ( $V_{in}$ ), the output voltage ( $V_{out}$ ) was compared to the theoretically expected voltage. The resistors  $R_{t1} = 1 \text{ M}\Omega$  and  $R_{t2} = 10 \text{ k}\Omega$  were defined so that the output voltage reaches high values (as expected for the OA1 of Figure 5.2) without the need of a high input voltage.

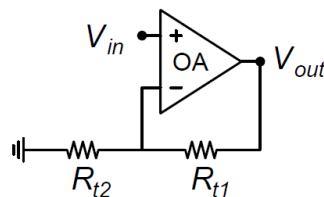


Figure 5.3 High-voltage operational amplifier experiment

The resulting resistors are displayed in Table 3. The transistors used in the circuit of Figure 5.3 are MPSA92 for all the PNP transistors and KSP42 for the NPN one.

Table 3. High-voltage operational amplifier parameters

Parameter symbol	Value
$R_1$	1 M $\Omega$
$R_2$	10 k $\Omega$
$R_3$	2 k $\Omega$
$R_4$	1 M $\Omega$

The experiments demonstrated that the circuit of Figure 5.2 is able to operate successfully over a range of  $\pm 240$  V. For higher values, the voltage across the transistor are close to their limits and the output voltage ( $V_{out}$ ) saturates.

### 5.3 Description of the Experimental Apparatus and Simulation Procedure

The experiments were conducted at the Laboratory of Aeroelasticity of the Department of Aeronautical Engineering of the São Carlos School of Engineering (University of São Paulo, Brazil). In this section, the apparatus, instrumentation and experimental tests are described.

Figure 5.4 shows the blower wind tunnel with nozzle of 500 x 500 mm that is employed during the experimental tests. A Pitot tube associated with a micromanometer (Trust Science Innovation) is installed in the tunnel. Temperature and pressure are measured by using a weather station (Instrutemp) and used to calculate the airflow speed.



Figure 5.4 Blower wind tunnel

Figure 5.5 and Figure 5.6 shows the experimental apparatus used for representing the typical section. The typical section shaft is mounted to metal plates on

its upper and the lower ends through bearings. Each side of both plates is connected to the fixed support by an elastic beam. The plunge stiffness is due to the four elastic beams. Therefore, the experimental setup in this work slightly deviates from the theoretical definition of a typical section (that assumes that springs do not contribute to system mass), yielding the fixture mass ( $m_f$ ) defined in Equation (3.2).

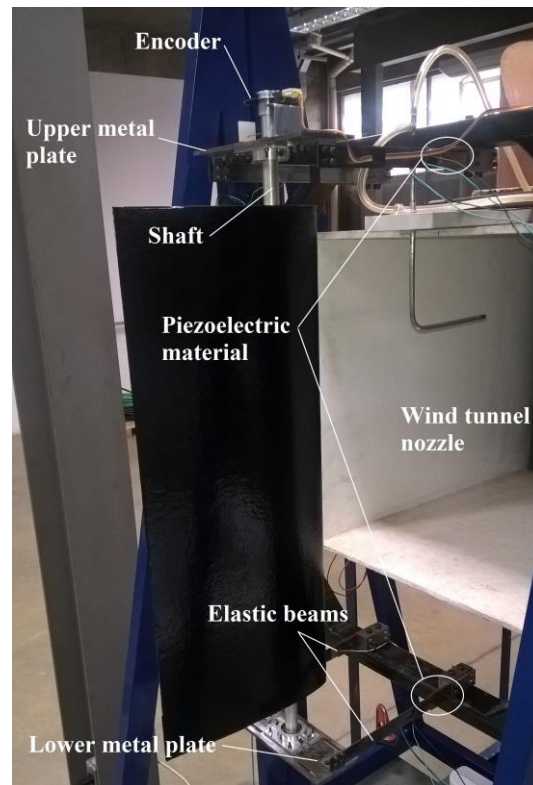


Figure 5.5 Two degree of freedom typical section during wind tunnel tests

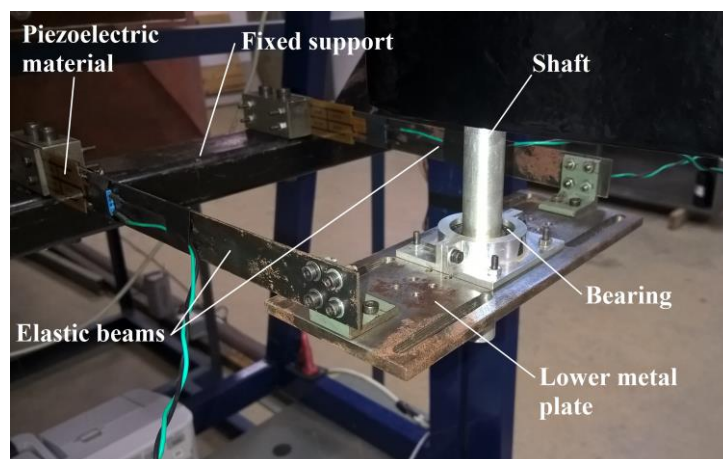


Figure 5.6 Connection of the typical section to the fixed support – lower end

The plunge displacement is measured with a strain gage, a CEA-13-240UZ-120 from Micro-Measurements (Vishay Precision Group). The strain gage is bonded on one

of the beams of the plunge DOF and connected to an HBM MGCplus AB22A amplifier system (Hottinger Baldwin Messtechnik). The calibration curve of the strain gage is adjusted by measuring the electrical signal from the sensor for no displacement and for a known displacement. One analogue output of the HBM system (the BNC connector at the front panel, Vo1) is adjusted to a range of  $\pm 10$  V as the plunge displacement (related to the strain gage deformation) is in a range of  $\pm 50$  mm.

The pitch stiffness is given by the spring wire that connects the shaft on the upper metal plate using a "L" corner, as shown in Figure 5.7. The free play can be added to the system through the "L" corner by increasing the spring wire hole diameter. A two-channel HEDS-9000 optical incremental encoder (Avago Technologies) with a two-inch HEDS-9000-T00 codewheel (US Digital) is used to measure the pitch angle. The codewheel has 2000 counts per revolution.



Figure 5.7 Pitch detail – upper end

The encoder signal (pitch angle) is driven to a dSPACE MicroLabBox controller board through a digital input channel. The HBM system analogue output (plunge displacement) is connected to one of the analogue inputs of the dSPACE system. The MATLAB/Simulink and ControlDesk softwares are used for controlling the data acquisition. The Simulink parameters are set as: fixed step solver, discrete time, no block reduction and no block reuse. The other parameters are kept in the "auto" mode. The dSPACE system scales its analogue input by a factor of 0.1, yielding an input signal between -1 V and +1 V when read by the Simulink model. Thus, the signals are corrected in the Simulink model.



Figure 5.8 Piezoceramics

Two piezoceramics (QP10N from Mide Corp.) are considered symmetrically in the plunge DOF (one in an upper beam and other in a lower beam, both in the same side, as in Figure 5.5) to avoid transversal rotation of the shaft. With the analytical model presented by ERTURK and INMAN (2009), the equivalent capacitance is obtained as  $C_p = 120$  nF and the electromechanical coupling parameter as  $\theta = 1.55$  mN/V. The typical section parameters are experimentally identified as described in Appendix A and are shown in Table 4.

Table 4. Typical section parameters

Parameter	Symbol	Value
Span length	$l$	0.5 m
Semichord	$b$	0.125 m
Nondimensional distance from elastic axis to mid-chord	$a$	-0.5
Nondimensional distance from elastic axis to CG	$x_\alpha$	0.2064
Airfoil mass	$ml$	0.804 kg
Fixture mass	$m_f l$	1.060 kg
Moment of inertia about the elastic axis	$I_\alpha l$	0.0028 kg.m <sup>2</sup>
Plunge stiffness	$K_h l$	2100 $\frac{\text{N}}{\text{m}}$
Pitch stiffness	$K_\alpha l$	2.65 $\frac{\text{Nm}}{\text{rad}}$
Plunge damping coefficient	$B_h l$	1.8770 $\frac{\text{N.s}}{\text{m}}$
Pitch damping coefficient	$B_\alpha l$	0.0199 $\frac{\text{N.m.s}}{\text{rad}}$

In this section, the simulations are performed considering the typical section equivalent electrical model (Figure 3.5). Besides the values from Table 4, it is necessary to obtain the real and imaginary components of Theodorsen's function, as described in section 3.1.2. For a determined value of wind speed  $U$ , the reduced frequency is calculated. The natural frequency  $f_n = 5.7$  Hz used in this step is obtained for the experimental system. For sinusoidal motion, Theodorsen's function can be evaluated in terms of Bessel functions of the first and second kind (THEODORSEN, 1935), which can be obtained directly from MATLAB. Finally, the derivatives can be obtained from Equation (3.22) and used to calculate the values of the electrical components of Figure 3.5.

The numerical simulations are performed for  $\rho = 1.07 \text{ kg/m}^3$  and for an initial displacement in the plunge DOF ( $h_i$ ) as initial condition. In the electrical equivalent model, the initial displacement is represented by an initial charge  $q_{h_i}$  in the plunge capacitor ( $C_h$ ). To apply this condition in Simulink, it is necessary to calculate the initial voltage  $V_i$  associated to  $q_{h_i}$ :

$$V_i = \frac{q_{h_i}}{C_h} \sim \frac{h_i}{C_h} \quad (6.1)$$

Moreover, in the simulations, the solver *ode15s* is used with maximum step size of 0.0001, relative tolerance of  $10^{-7}$ , absolute tolerance of  $10^{-6}$  and an adaptive algorithm. The other parameters are kept in the “auto” mode. Simulations are performed in short circuit condition or considering the nonlinear shunt circuit in the electrical domain of the equivalent model. The general steps followed in the simulations are represented in the flow chart of Figure 5.9.

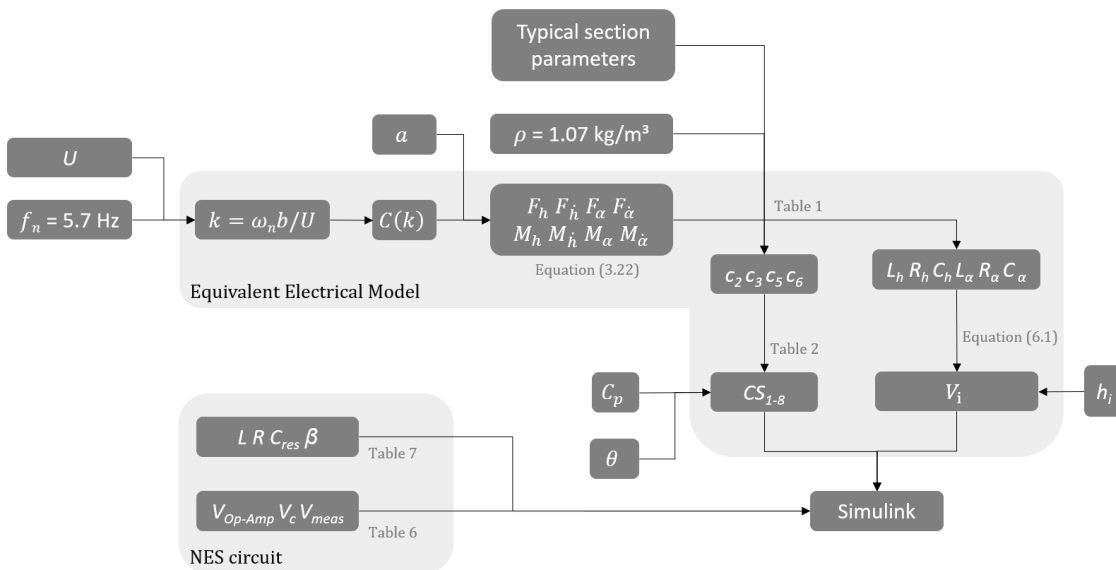


Figure 5.9 Simulation flow chart

#### 5.4 Reference Case

The aeroelastic behavior of the typical section with the piezoelectric material in short-circuit (SC) condition is assumed as a reference case. Although piezoelectric material is present (in terms of mass and stiffness), the behavior is equivalent to an electromechanically uncoupled system. The time responses of pitch and plunge DOFs are numerically evaluated for different airflow speeds and the short-circuit flutter speed

of the typical section is then determined. The simulations showed that the system is stable for airflow speeds smaller than 9.7 m/s and unstable for airflow speed larger than 9.9 m/s as displayed in Figure 5.10. Therefore, the numerical short-circuit flutter speed is assumed as 9.8 m/s.

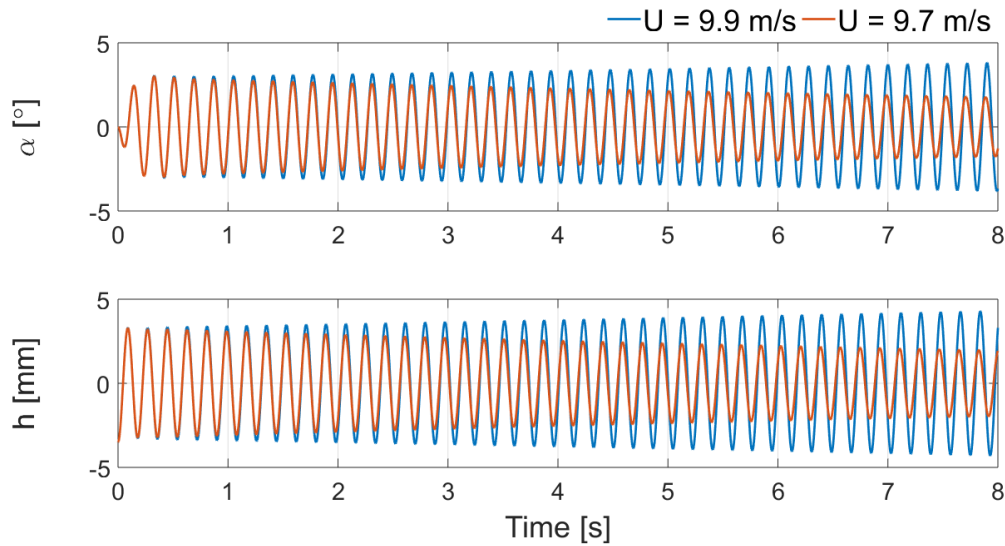


Figure 5.10 Numerical time responses of pitch and plunge displacements at airflow speeds around the numerical short-circuit flutter speed (9.8 m/s) for the linear typical section at SC condition

The numerical predictions are then verified with experimental data from wind tunnel tests. The experimental short-circuit flutter speed is 10.8 m/s, 10.2 % higher than the numerical one. Figure 5.11 displays the numerical and experimental time responses for the correspondent flutter speed, or 9.8 m/s for the numerical and 10.8 m/s for the experimental one. The numerical flutter frequency is 5.55 Hz while the experimental one is 5.65 Hz (1.8 % higher).

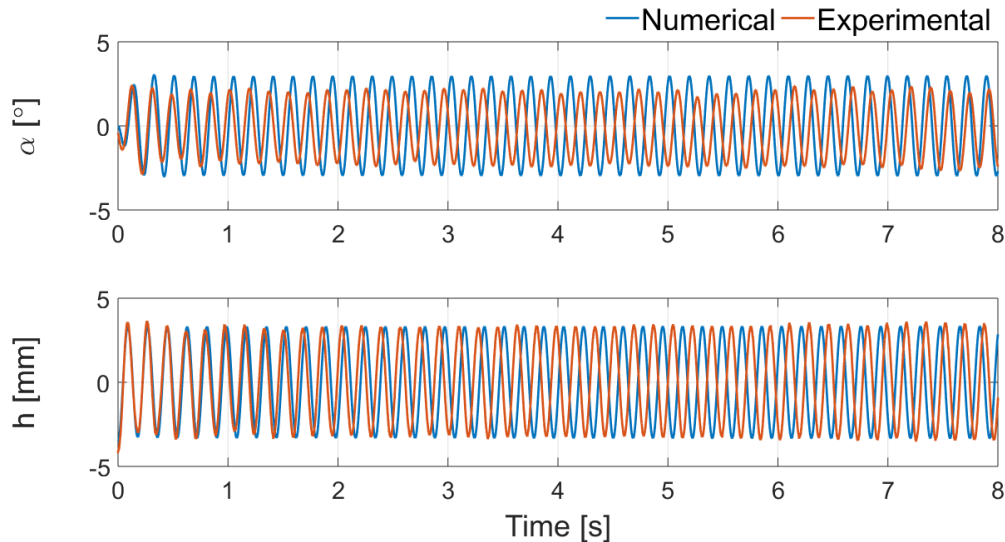


Figure 5.11 Numerical and experimental time responses of pitch and plunge displacements at the correspondent short-circuit flutter speed (9.8 m/s for the numerical and 10.8 m/s for the experimental) for the linear typical section at SC condition

To investigate the difference between numerical and experimental flutter speed, the system response was numerically and experimentally verified for different airflow speeds and the comparisons are displayed in Figure 5.12.

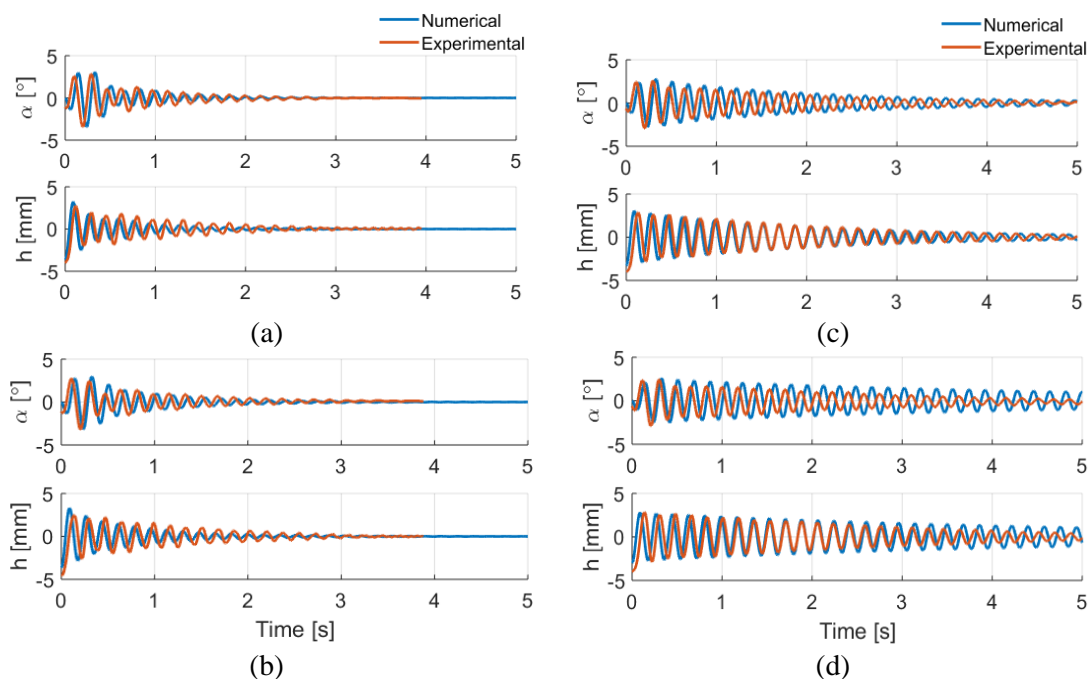


Figure 5.12 Numerical and experimental time responses of pitch and plunge displacements at (a) 3.9 m/s, (b) 6.7 m/s, (c) 8.9 m/s and (d) 9.5 m/s for the linear typical section at SC condition

From Figure 5.12, one can note that the amplitudes of the numerical and experimental curves are slightly different. Besides, for lower speeds, the decay rate of

the numerical curve is higher than the experimental one. However, as the speed increases, this behavior is reversed and the numerical decay rate becomes lower than the experimental, which results in a higher experimental flutter speed. Considering the various sources of error, from modeling to the imprecision of the experiment (which are discussed forward), the error between e experimental and numerical short circuit flutter speed is acceptable.

### 5.5 Linear Typical Section Combined to the Nonlinear Shunt Circuit

In this section, the effects of the piezoelectric based NES on the aeroelastic behavior of the typical section are verified numerically and experimentally. The maximum inductance value to be employed in the NES circuit is limited to 10 H in order to avoid the use of synthetic inductance circuits that would increase the complexity of the circuit and require additional external power. Moreover, the maximum voltage across the piezoelectric material is limited in the simulations to 200 V in order to avoid depolarization of the piezoelectric material and keep voltages inside the operation range of the high-voltage operational amplifier. Since the residual capacitance ( $C_{res}$ ) is related to the internal capacitance of the piezoceramic and the negative capacitance (please check Equation (4.4)), larger  $C_{res}$  is achieved when the negative capacitance cancels the internal capacitance of piezoceramics, or when  $C_{neg} \rightarrow -C_p$ ,  $C_{res} \rightarrow \infty$  in Equation (4.4), resulting in essentially nonlinear system. However, the complete cancellation of system linear capacitance would result in instability in experimental cases (what is not observed in numerical cases since ideal electrical elements are assumed). Therefore, the negative capacitance is always adjusted to cancel the internal capacitance and keep the system stability.

In order to adjust the NES circuit parameters in the simulations, the negative capacitance is assumed to cancel the linear capacitance. Then, simulations are performed to adjust the circuit inductance ( $L$ ), resistance ( $R$ ) and the nonlinear capacitance ( $\beta$ ) that yields enhanced vibration attenuation. As the nonlinear attachment still works as a NES for small enough values of linear stiffness (SILVA et al., 2018; ZHOU; THOUVEREZ; LENOIR, 2014), there is an optimum value of  $C_{res}$  in the numerical and experimental cases that avoids extremely large voltages across the piezoelectric material electrodes and yields targeted energy transfer. Experimental tests with the negative capacitance circuit (Figure 4.5) are performed to obtain the acceptable negative capacitance in the stable domain (that is also assumed in the simulations).

Lastly, if the voltage across the piezoelectric material still needs to be reduced, the resistor  $R$  can be adjusted (increased). The adjusted NES parameters  $L$ ,  $R$ ,  $C_{res}$  and  $\beta$  are input values for obtaining the NES circuit elements according section 4.1. In this step, the maximum voltages considered in different parts of the circuit are displayed in Table 5.

Table 5. Maximum design voltages

Voltage	Symbol	Maximum value
OpAmp voltage	$V_{Op-Amp}$	15 V
Cubic voltage	$V_c$	20 V
Multipliers input voltage	$V_{meas}$	9 V

The values of Table 5 were chosen according the limit voltage of the operational amplifiers (LM358) and voltage multipliers (AD633) used in the circuit of Figure 4.3. Besides, the maximum voltage for the piezoelectric material is obtained from the maximum voltage for  $V_c$  (please check Figure 4.2) as:

$$V_{p_{max}} = \frac{q_{p_{max}}}{c_p} = \frac{1}{c_p} \sqrt[3]{\frac{V_{c_{max}}}{\beta}} . \quad (6.2)$$

It is important to note that the NES performance depends on the plunge initial condition (CATALDO; BELLIZZI; SAMPAIO, 2013) so all the parameters are adjusted for an initial plunge displacement of 3 mm. The final properties of the NES are shown in Table 6.

Table 6. NES final parameters

Parameter	Symbol	Value
NES inductor	$L$	10 H
NES resistor	$R$	330 k $\Omega$
Residual capacitance	$C_{res}$	50 $\mu$ F
Nonlinear capacitance term	$\beta$	500 $\frac{TV}{C^3}$

Using the parameters of Table 6, the voltage-charge behavior of the linear residual capacitance ( $q/C_{res}$ ), the cubic capacitance ( $\beta q^3$ ) and the combined one were

obtained numerically. Figure 5.13 shows that, although a residual capacitance is present, the resulting voltage-charge behavior is very close to a cubic one, what is enough to enable an essential nonlinear behavior. To verify the experimental voltage-charge behavior, the cubic voltage  $V_c$  measured during the experiments is display along with the numerical curve in Figure 5.14.

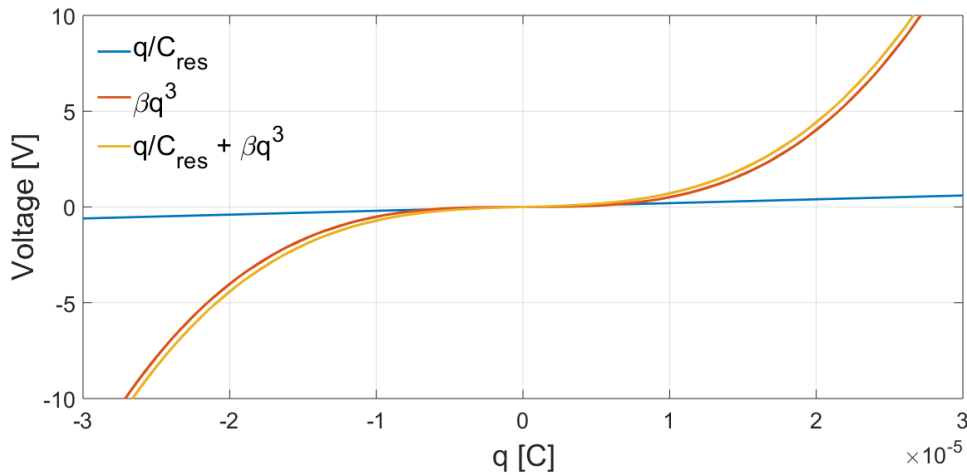


Figure 5.13 Voltage-charge behavior for the linear typical section with NES

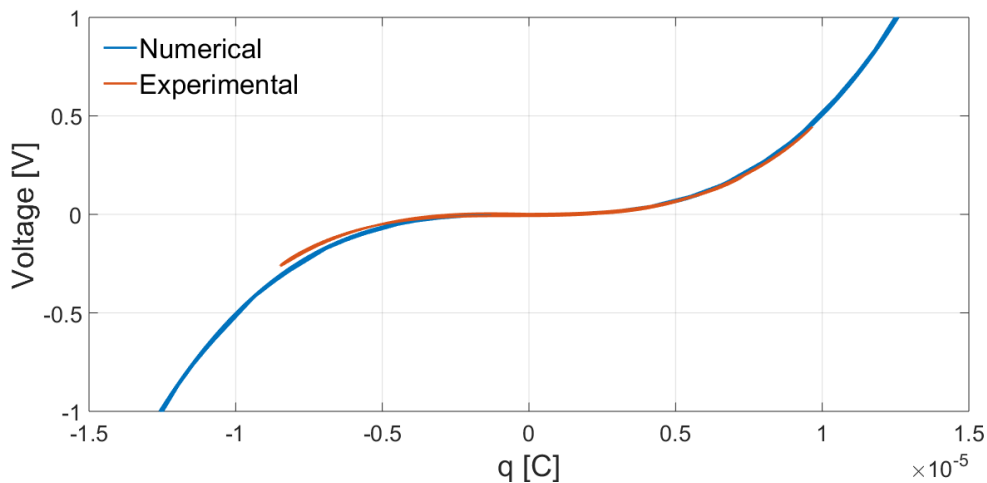


Figure 5.14 Nonlinear voltage-charge behavior for the linear typical section with NES

The effects of the piezoelectric NES in the typical section is then analyzed numerically. The aeroelastic behavior of the typical section connected to the NES is compared to the reference case through the time response for pitch ( $\alpha$ ), plunge ( $h$ ), the voltage across the piezoelectric material ( $V_p$ ) and the cubic voltage ( $V_c$ ). The aeroelastic behavior displayed in Figure 5.15 is obtained at numerical short-circuit flutter speed. While persistent oscillations are observed for the short-circuit condition, the use of

piezoelectric based NES results in damped oscillations. In such case, the maximum voltage across the piezoceramic electrodes is 121.7 V.

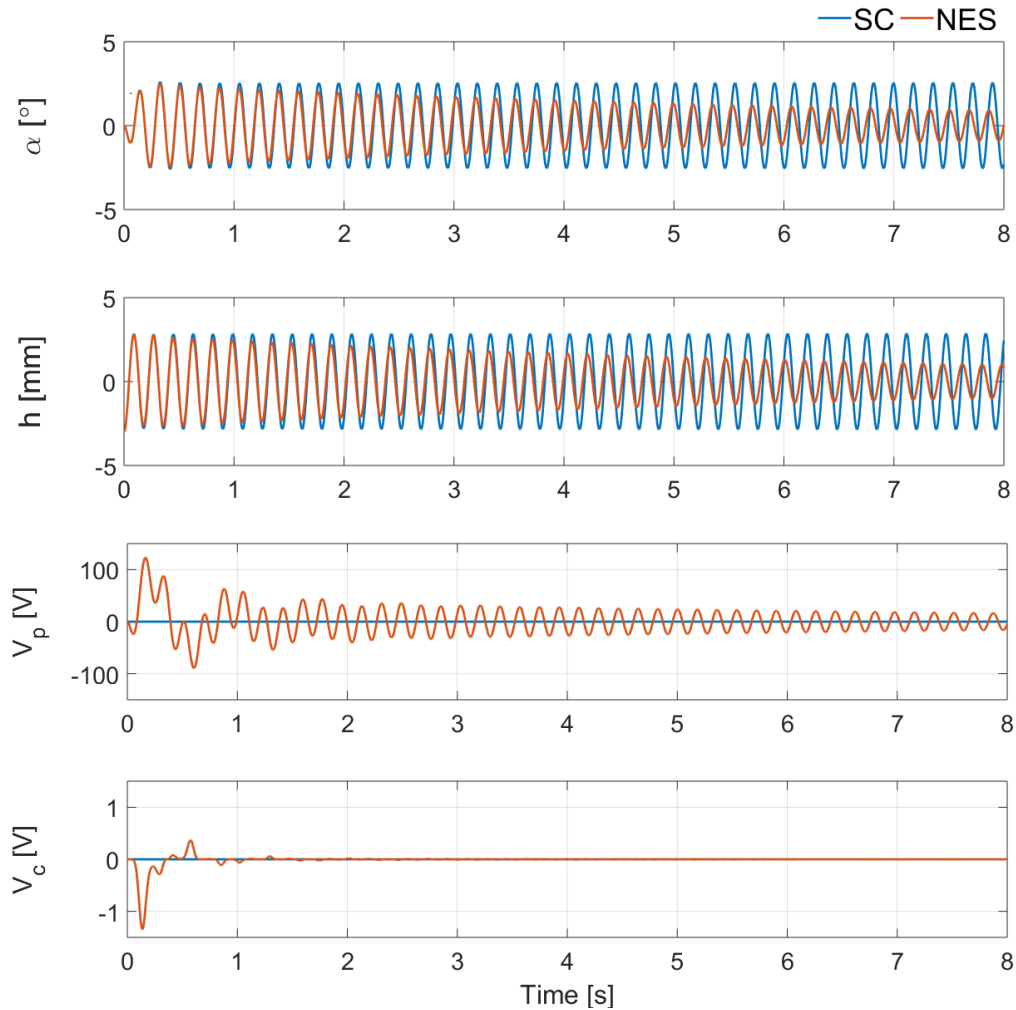


Figure 5.15 Numerical effects of piezoelectric NES at numerical short-circuit (SC) flutter speed (9.8 m/s) for pitch and plunge displacements, the voltage across the piezoelectric material and the cubic voltage for the linear typical section

Figure 5.16 displays the time response for pitch ( $\alpha$ ), plunge ( $h$ ), the voltage across the piezoelectric material ( $V_p$ ) and the cubic voltage ( $V_c$ ) at different airflow speeds above linear short-circuit flutter speed. In such case, the system is stable for airflow speeds smaller than 10.1 m/s, assumed as the new flutter boundary that is 3.1 % larger than the short-circuit one. The maximum voltage across the piezoceramic electrodes is smaller than 123.5 V for all stable cases.

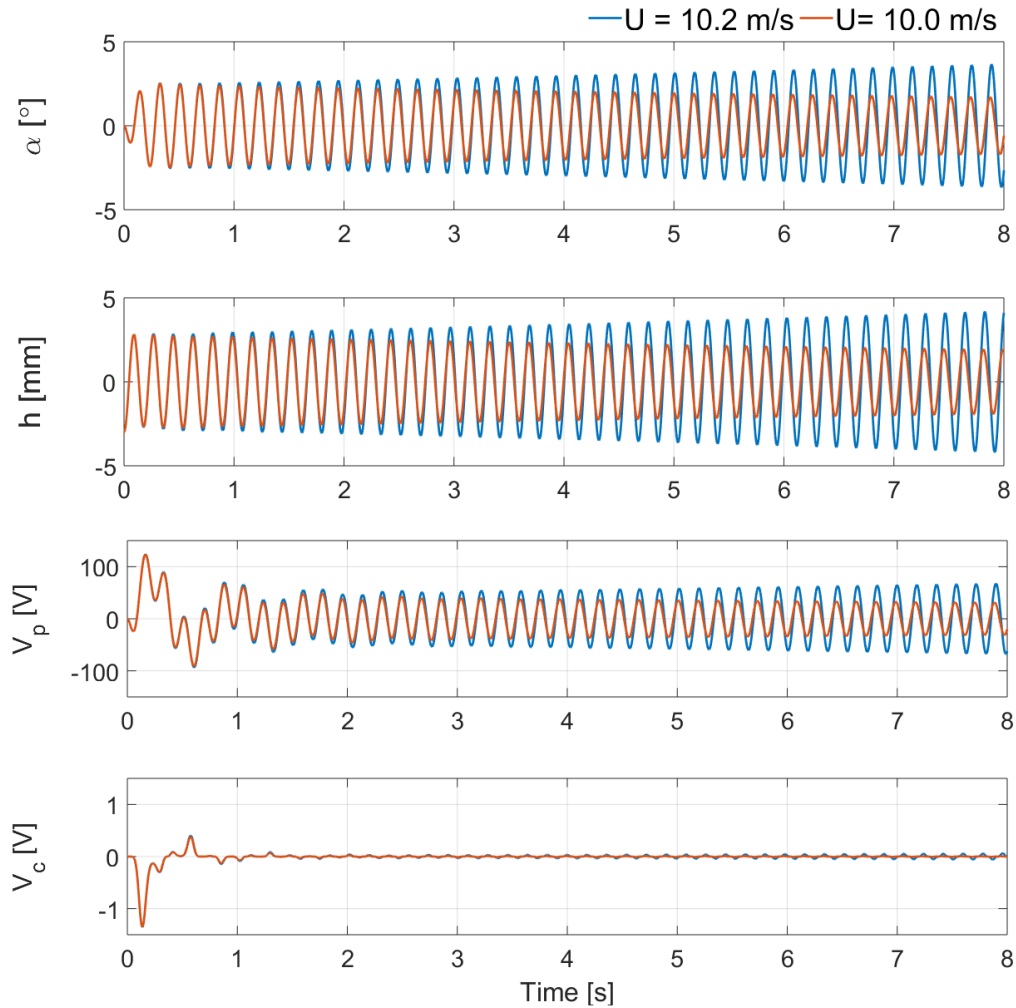


Figure 5.16 Numerical time responses of pitch and plunge displacements, the voltage across the piezoelectric material and the cubic voltage at airflow speeds around the numerical flutter speed (10.1 m/s) for the linear typical section with NES

Wind tunnel tests have also been performed in order to verify the numerical predictions. Figure 5.17 displays the experimental curve at the last stable curve, 11.2 m/s (assumed as the flutter speed) and numerical simulations at the numerical flutter speed (10.1 m/s), demonstrating that the experimental data follows the same trends of the numerical ones with similar amplitudes.

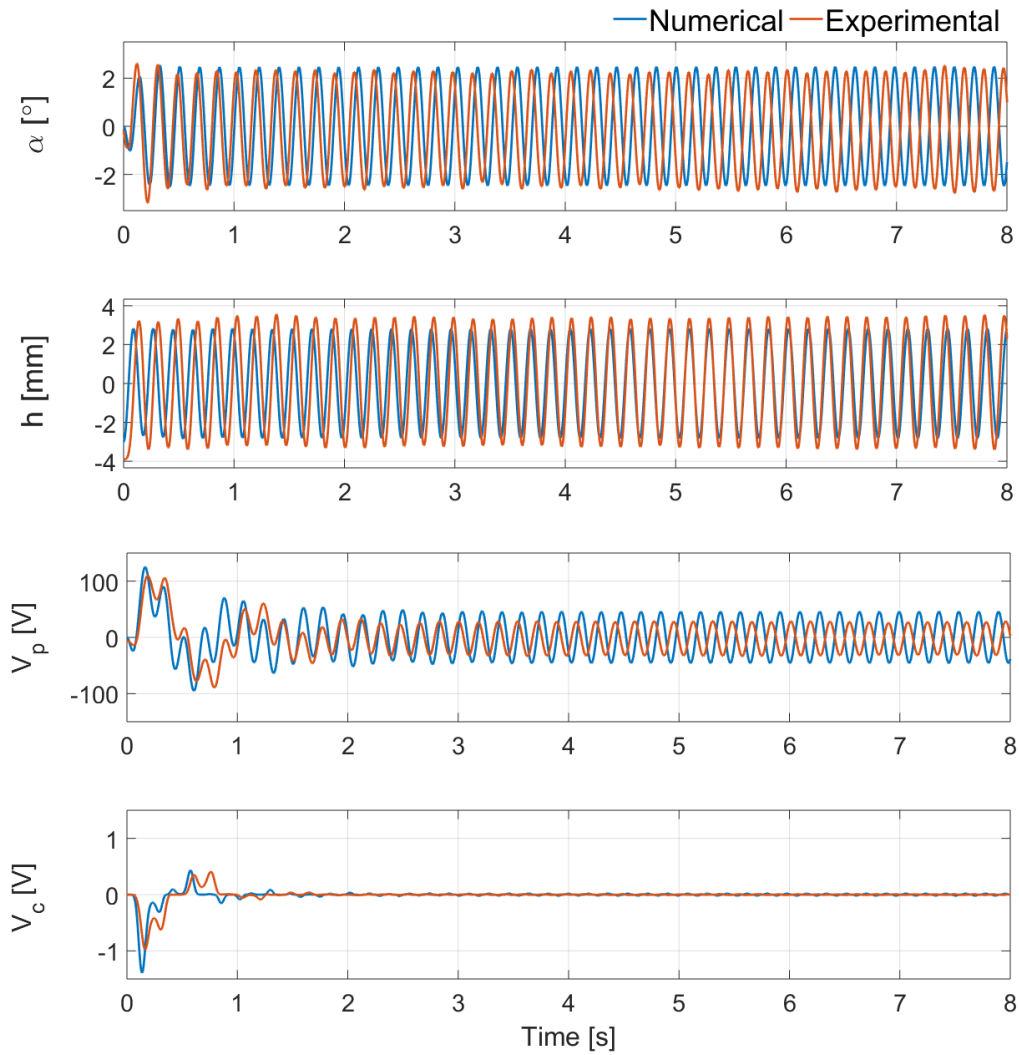


Figure 5.17 Numerical and experimental time responses of pitch and plunge displacements, the voltage across the piezoelectric material and the cubic voltage at the correspondent flutter speed (10.1 m/s for the numerical and 11.2 m/s for the experimental) for the linear typical section with NES

Then, the time frequency behavior is analyzed by using the wavelet transform. It allows the verification of temporal evolution of the frequency components of the signals. Figure 5.18 presents the wavelet transform applied to the typical section connected to the piezoelectric NES. Heavily shaded areas correspond to higher amplitudes. The plots represent the frequency of pitch ( $\alpha$ ), plunge ( $h$ ) and voltage across the piezoelectric material ( $V_p$ ) as a function of time.

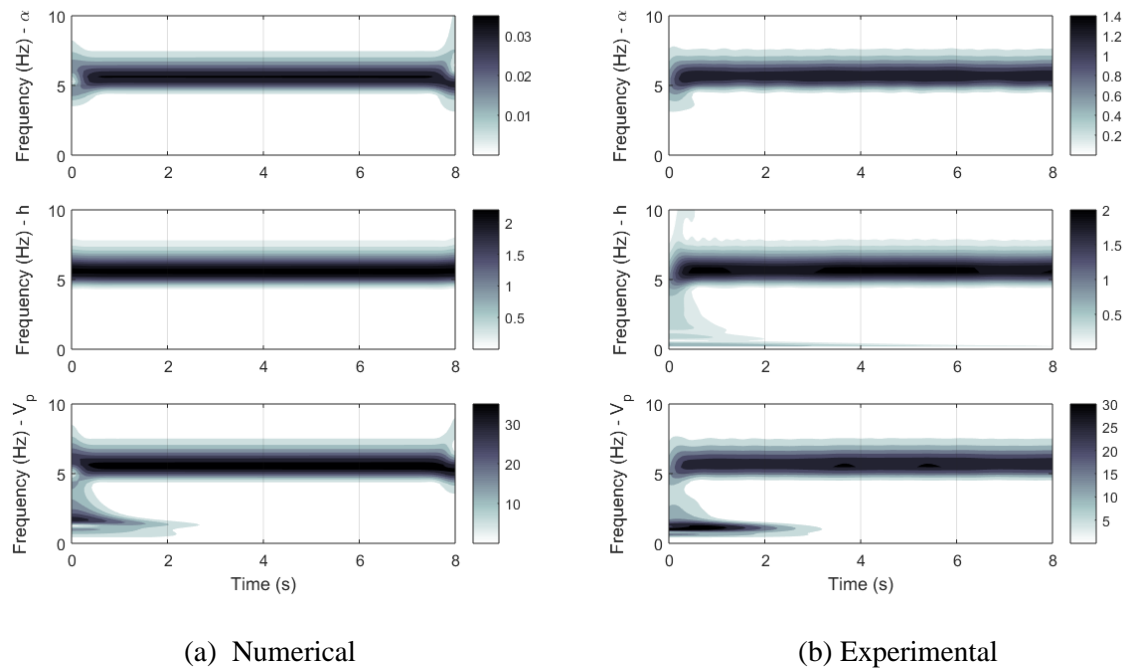


Figure 5.18 Numerical and experimental wavelet transform at the correspondent flutter speed (10.1 m/s for the numerical and 11.2 m/s for the experimental) for the linear typical section with NES

Figure 5.18 shows that the response of the typical section connected to the piezoelectric NES presents two distinct frequencies for the displayed time. The dominant frequency corresponds to the flutter frequency (5.7 Hz), which is present during the whole analysis and the lower frequency, which is present only during transient period and is caused by the electrical domain of the system. Figure 5.18 also shows that the compositions of numerical and experimental behavior are similar. The overall agreement between the numerical and experimental results both in time and frequency domain is considered acceptable and enough to validate the linear typical section equivalent model and the NES circuit.

The effects of the piezoelectric based NES are also discussed numerically in terms of energy. The total energy of the system is due to kinetic, potential and electrical energies and is presented as:

$$\begin{aligned}
E_{sis} = & \left[ \frac{1}{2}(m + m_f)l\dot{h}^2 + \frac{1}{2}I_\alpha l\dot{\alpha}^2 + S_\alpha l\dot{h}\dot{\alpha} \right]_{kinetic} + \left[ \frac{1}{2}K_h l\dot{h}^2 \right. \\
& \left. + \frac{1}{2}K_\alpha l\dot{\alpha}^2 \right]_{potential} + \left[ Lq_p^2 + \frac{1}{2}\frac{1}{C_{res}}q_p^2 \right. \\
& \left. + \frac{1}{2}\beta q_p^4 \right]_{electrical}
\end{aligned} \tag{6.3}$$

where gravitational effects are not taken into account. The mechanical dampers of each DOF of the typical section and the resistor of the NES are responsible for energy dissipation, which is defined as:

$$ED = \left[ \int B_h l\dot{h}^2 dt + \int B_\alpha l\dot{\alpha}^2 dt \right]_{mechanical} + \left[ \int Rq_p^2 dt \right]_{electrical} \tag{6.4}$$

The input energy ( $E_{in}$ ) is the sum of the initial energy due to the initial conditions ( $E_{sis}(0)$ ) and the nonconservative work due to the unsteady aerodynamic loads ( $W_{nc}$ ):

$$E_{in}(t) = W_{nc}(t) + E_{sis}(0) = E_{sis}(t) + ED(t) \tag{6.5}$$

Figure 5.19 displays the energy terms for the typical section in short-circuit condition and for the typical section connected to the NES, both at the airflow speed of 9.8 m/s (numerical short-circuit flutter speed). For the short-circuit case, the dampers of each mechanical DOF are the only elements that dissipate energy. Although the damper continuously dissipates energy at rate that is comparable to the average rate of increase of the energy input due to the airflow, this is not enough to effectively damp flutter oscillations and the instantaneous total energy ( $E_{sis}$ ) remains almost constant along time. Therefore, the self-sustained oscillations of Figure 5.15 are observed. On the other hand, the energy dissipated by piezoelectric based NES increases along time, balancing the energy input from the airflow and, ultimately, suppressing flutter oscillations after a few seconds.

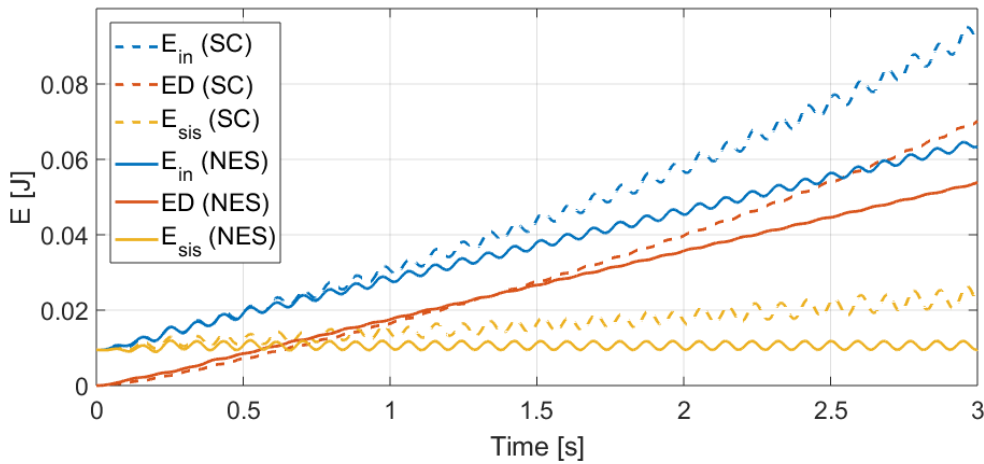


Figure 5.19 Input energy, dissipated energy and energy in the system at numerical short-circuit flutter speed (9.8 m/s)

The energy flow from the mechanical to the electrical domain of the system can be calculated as:

$$P_h = -\frac{\theta V_p}{l} \dot{h} \quad (6.6)$$

that is displayed in Figure 5.20. Despite some regions of negative values of power, Figure 5.20 shows that energy flows from mechanical to electrical domain mostly in a one-way fashion, as expected in target energy transfer due to essentially nonlinear attachments.

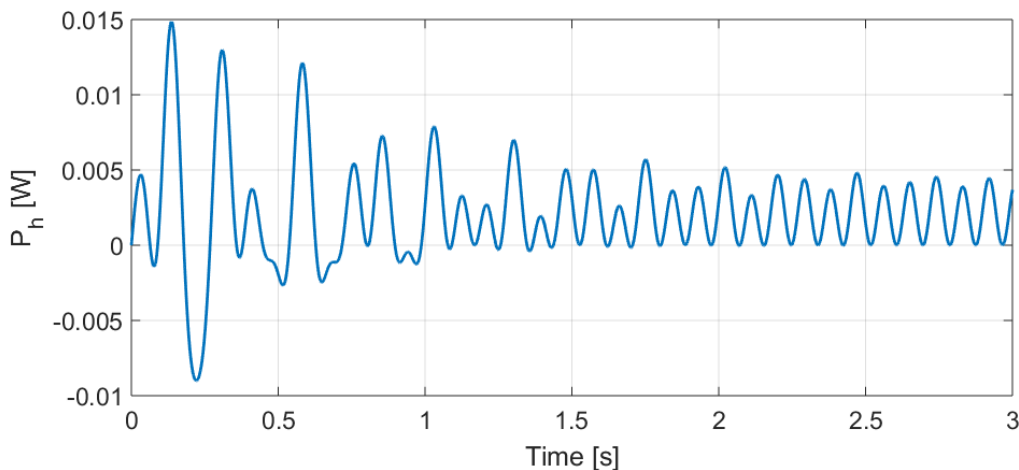


Figure 5.20 Power flowing from the mechanical to the electrical domain for at numerical short-circuit flutter speed (9.8 m/s)

One of the most interesting properties of essentially nonlinear attachments is the robustness against detuning. Therefore, Figure 5.21 displays the variation of flutter

speed of the typical section with changing properties (center of gravity  $x_a$  and inertia of each DOF and stiffness of each DOF) for the short-circuit condition and for the piezoelectric based NES. Each property was individually multiplied by a factor  $\gamma$ . From Figure 5.21, one can note how the parameters affect the NES performance. For example, the blue curve indicates that moving the center of gravity towards the leading edge (decreasing  $x_a$ ), closer to the axis of rotation, would decrease the flutter speed of the SC condition, but increase the flutter speed with the NES, which indicates a better performance of the NES. A similar behavior can be seen for the other parameters, excepting the moment of inertia about the elastic axis, which behaves in opposition. However, the flutter speed with the piezoelectric based NES is always higher than the short-circuit flutter speed for the range of parameters considered in Figure 5.21. Since the same NES parameters were considered in all cases, Figure 5.21 shows the robustness of the nonlinear attachment against detuning.

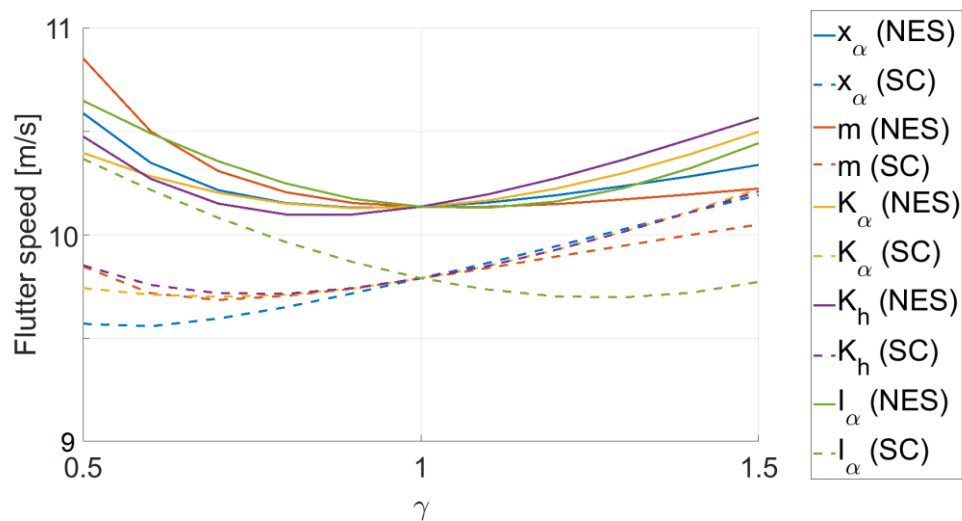


Figure 5.21 Flutter speed against the factor  $\gamma$

## 6 Effects of Piezoelectric Based NES on the Aeroelastic Behavior of the Nonlinear Typical Section

This section presents the numerical and experimental verification of the aeroelastic behavior of the electromechanically coupled system considering the nonlinear typical section. The simulations are performed replacing the pitch circuit of the typical section equivalent electrical model (Figure 3.5) by equivalent circuit of Figure 3.6. As in the linear case, the typical section parameters are displayed in Table 4 and the general steps followed in the simulations are represented in the flow chart of Figure 5.9.

Experimentally, the free play gap is added to the typical section through the "L" corner displayed in Figure 5.7. As mentioned before, the free play gap is the result of increasing the spring wire hole diameter. In this work, the hole diameter is equivalent to a semi free play gap ( $\alpha_{fp}$ ) estimated as 0.4 degrees.

### 6.2 Reference Case

The aeroelastic behavior of the typical section with the piezoelectric material in short-circuit (SC) condition is again assumed as a reference case. Considering the numerical nonlinear 2-DOF typical section with a semi free play gap ( $\alpha_{fp}$ ) of 0.4 degrees and an initial plunge displacement of 3 mm, limit cycle oscillations (LCO) were observed for airflow speeds from 9.5 m/s to 9.8 m/s with different amplitudes in the permanent region, as displayed in Figure 5.10. It can be noted that the increase of the airflow speed has a significant effect in the amplitude of oscillation, which can reach values that are impracticable in the experiments.

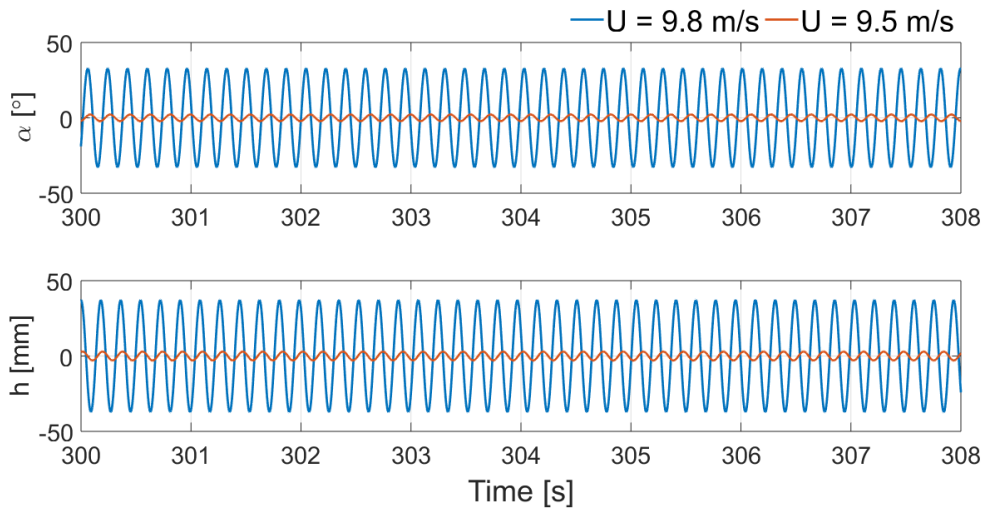


Figure 6.1 Numerical time responses of pitch and plunge displacements at airflow speeds around the numerical range of LCO for the nonlinear typical section at SC condition

The numerical predictions are then verified with experimental data from wind tunnel tests. During the experimental tests, values of plunge initial displacement up to 4 mm were insufficient to trigger limit cycle response. However, for higher values, the development of the LCO was very consistent. LCO was observed over a narrow range of speeds around 11.0 m/s. Figure 5.11 displays the numerical and experimental time responses for the correspondent speed, or 9.5 m/s for the numerical and 11.0 m/s for the experimental one (14 %).

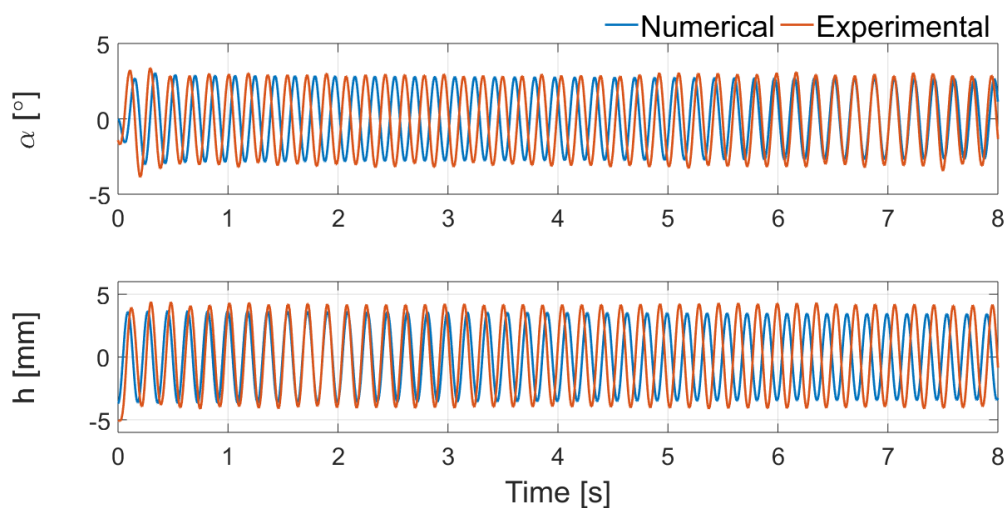


Figure 6.2 Numerical and experimental nonlinear time responses of pitch and plunge displacements at the speed above which LCO is observed (9.5 m/s for the numerical and 11.0 m/s for the experimental) for the nonlinear typical section

The difference between numerical and experimental behavior, measured by the difference in the flutter speed, was slightly higher for the nonlinear case, but can be

justified by the additional source of nonlinearity compared to the linear typical section case presented in section 5.4.

### 6.3 Nonlinear Typical Section Combined to the Nonlinear Shunt Circuit

The effect of the piezoelectric based NES is verified by comparing the numerical aeroelastic behavior of the reference case and the NES case at the speed in which LCO starts to occur for SC case (9.5 m/s). Figure 6.3 displays the time response for pitch ( $\alpha$ ), plunge ( $h$ ), the voltage across the piezoelectric material ( $V_p$ ) and the cubic voltage ( $V_c$ ) for both conditions (SC and NES).

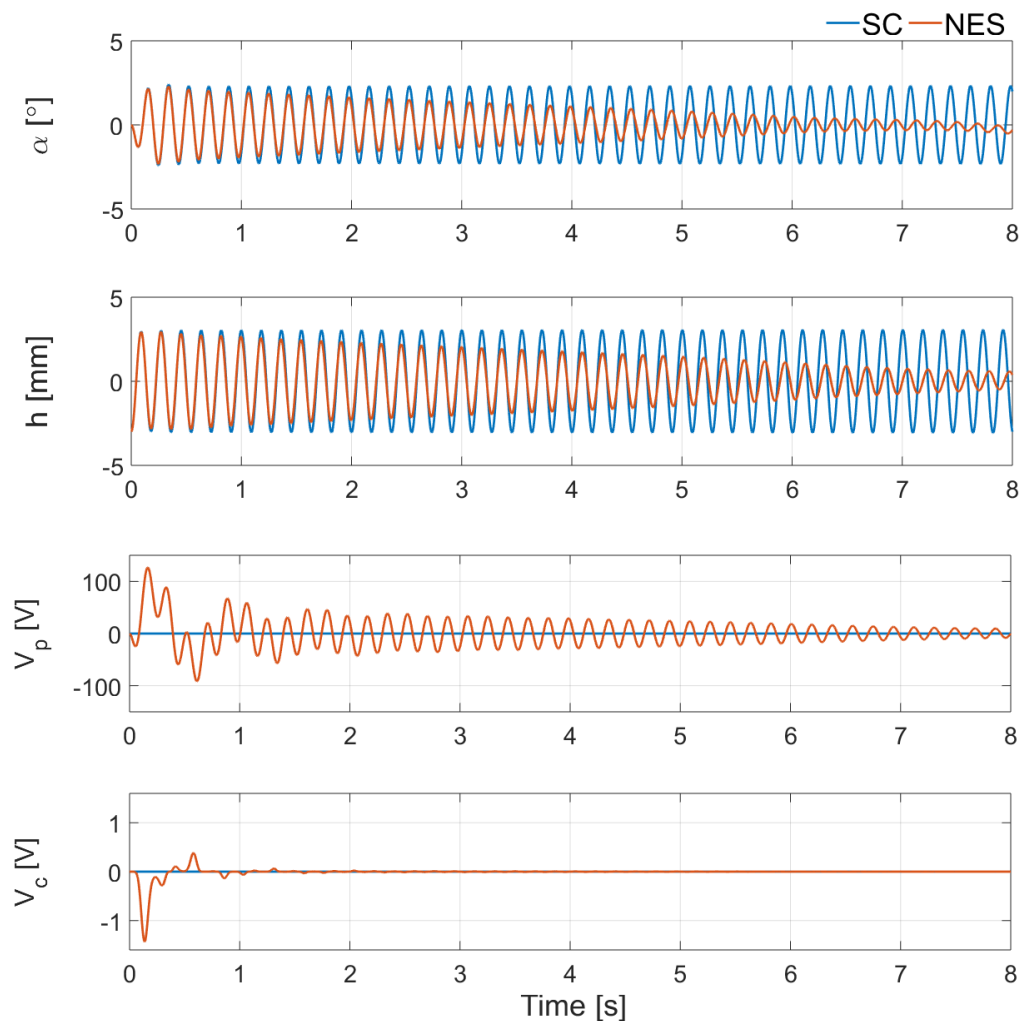


Figure 6.3 Numerical effects of piezoelectric NES at 9.5 m/s for pitch and plunge displacements, the voltage across the piezoelectric material and the cubic voltage for the nonlinear typical section

Connecting the piezoelectric based NES, the nonlinear attachment is able to damp the oscillations (Figure 6.3), expanding the stability boundary to 9.9 m/s. It is important to note that LCO are not observed when the piezoelectric NES is added and,

for airflow speed under 9.9 m/s, the oscillations are completely suppressed, otherwise, the system is unstable and oscillations with increasing amplitudes are observed. Figure 6.4 displays the time response for pitch ( $\alpha$ ), plunge ( $h$ ), the voltage across the piezoelectric material ( $V_p$ ) and the cubic voltage ( $V_c$ ) at different airflow speeds around the stability boundary. The maximum voltage across the piezoceramic electrodes is smaller than 127.3 V for all stable cases.

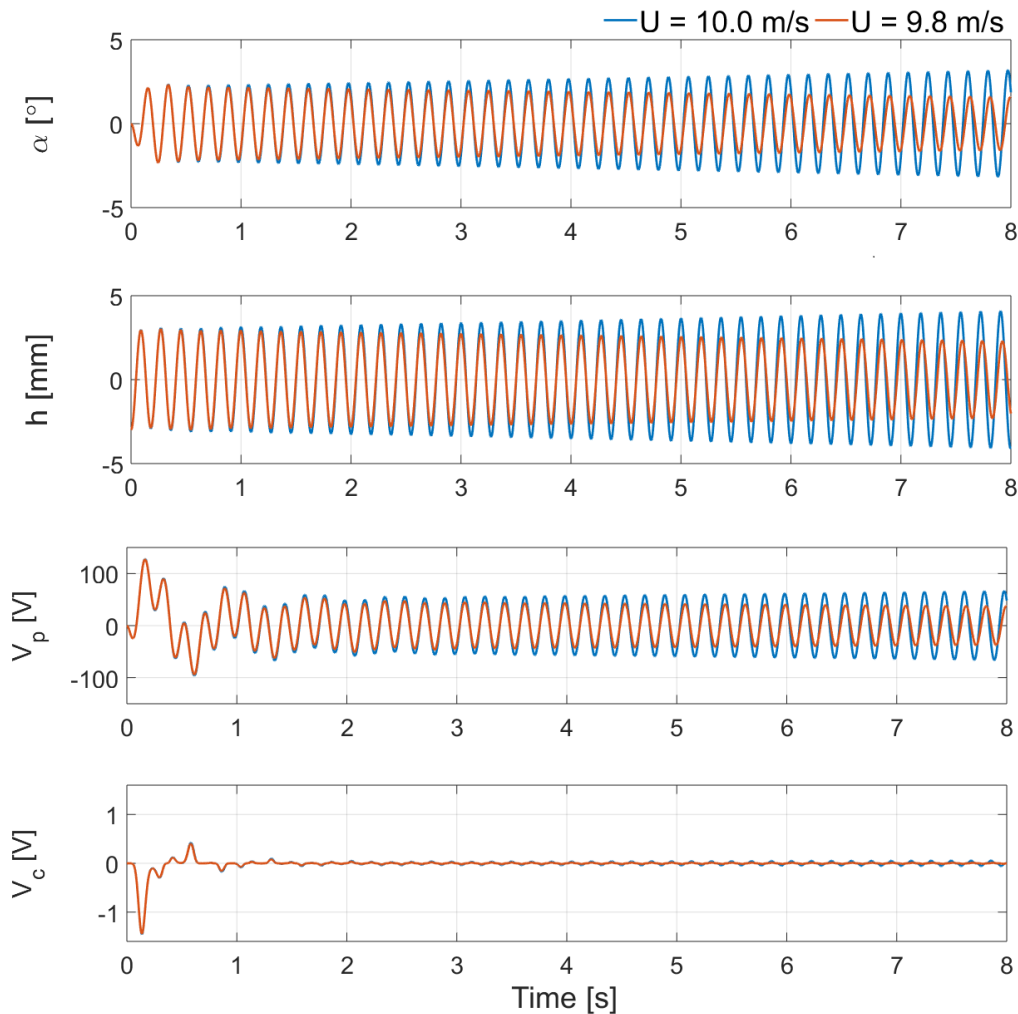


Figure 6.4 Numerical time responses of pitch and plunge displacements, the voltage across the piezoelectric material and the cubic voltage at airflow speeds around the stability boundary (9.9 m/s) for the nonlinear typical section

Wind tunnel tests have also been performed in order to verify the numerical predictions for the nonlinear typical section. Experimentally, the piezoelectric NES was able to expand the stability boundary to 11.3 m/s, as shown in Figure 6.5. Figure 6.5 demonstrates that, as in the linear case, despite some differences in the transient region, the experimental data follows the same trends of the numerical ones.

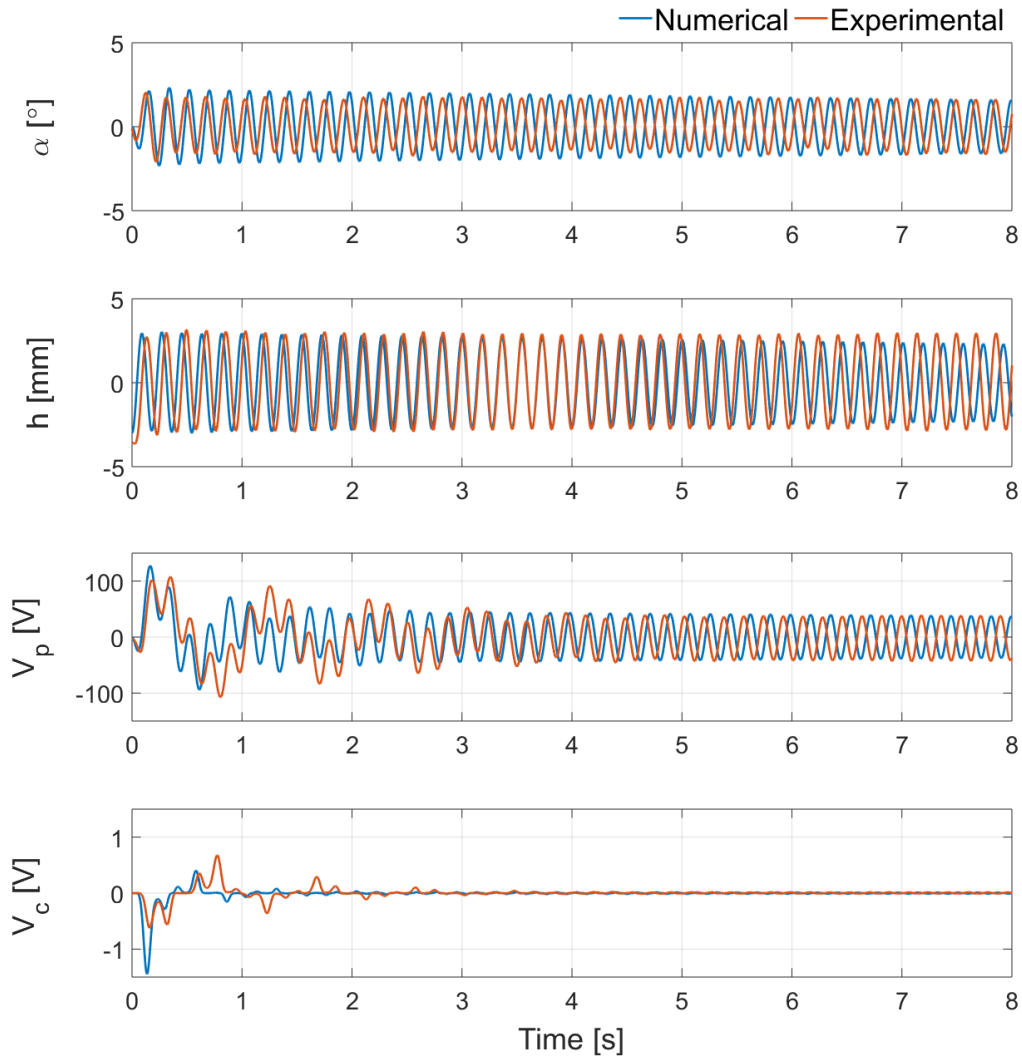


Figure 6.5 Numerical and experimental time responses of pitch and plunge displacements, the voltage across the piezoelectric material and the cubic voltage at the boundary stability speed (9.9 m/s for the numerical and 11.3 m/s for the experimental) for the nonlinear typical section

Finally, the wavelet transform is used to discuss time frequency behavior. Figure 6.6 presents the wavelet transform applied to numerical and experimental curves with the piezoelectric NES connected to the nonlinear typical section.

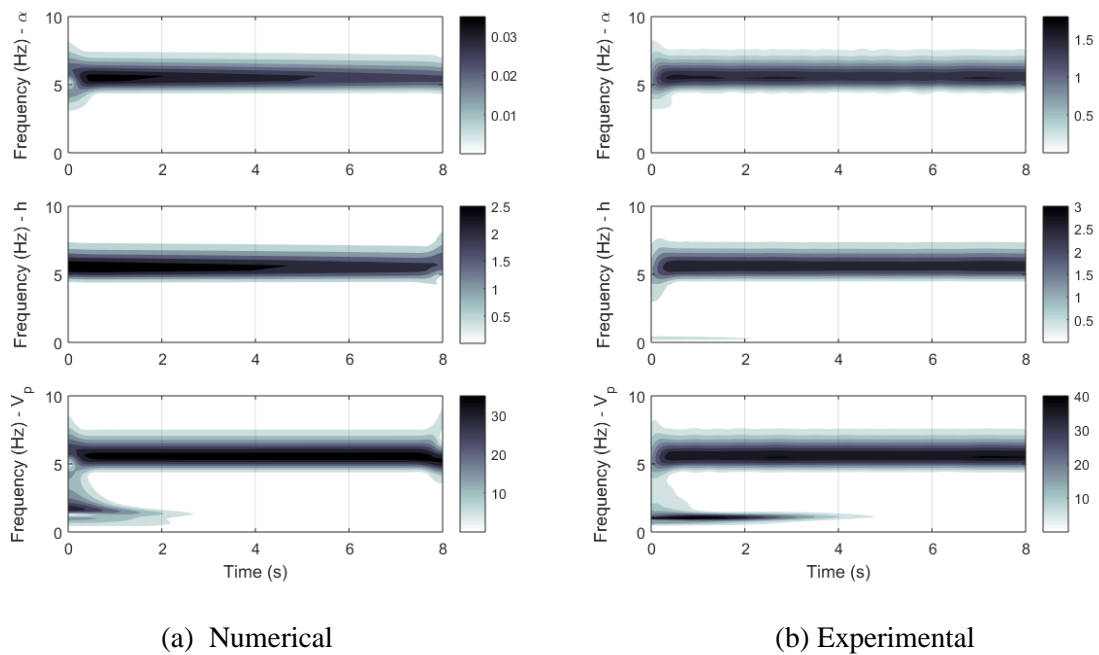


Figure 6.6 Numerical and experimental wavelet transform at the correspondent flutter speed (9.9 m/s for the numerical and 11.3 m/s for the experimental)

As in the linear case, Figure 6.6 shows two distinct frequencies in the system response: a dominant frequency, correspondent to the flutter frequency (5.7 Hz) and present during the whole analysis, and a lower frequency, from the electrical domain and characterizing the transient period. The frequency compositions for numerical and experimental curves displayed Figure 6.6 are similar and the overall agreement between the numerical and experimental results both in time and frequency domain demonstrates that the nonlinear typical section equivalent model represents adequately the physical system and as well as the NES circuit model.

The energy analysis presented for the linear case are applied to the nonlinear typical section. Figure 5.19 displays the energy terms presented in section 5.5 for the nonlinear typical section in short-circuit condition and connected to the NES, both at the numerical short-circuit flutter speed (9.5 m/s). The behavior is similar to the linear case.

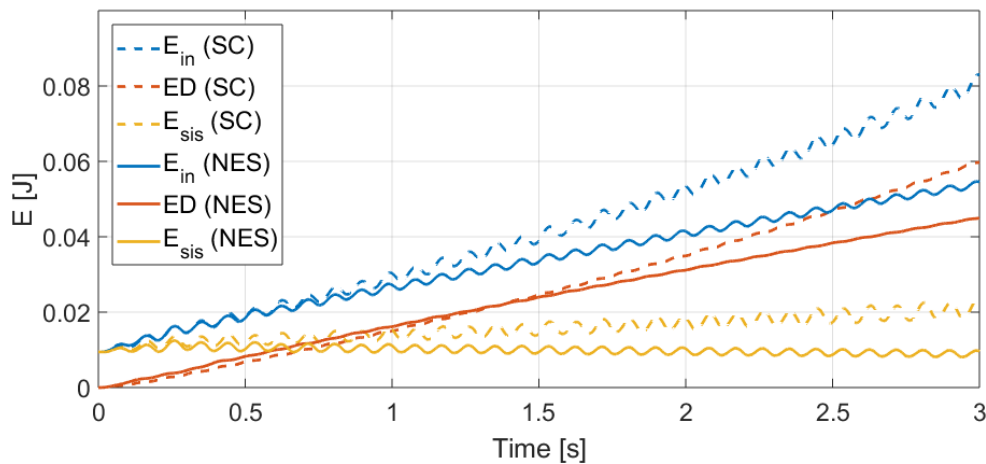


Figure 6.7 Input energy, dissipated energy and energy in the system at numerical short-circuit flutter speed (9.5 m/s)

The energy flow from the mechanical to the electrical domain of the system is displayed in Figure 5.20 and also displays a behavior similar to the linear case, demonstrating that, in terms of energy, no significant variation in the piezoelectric based NES behavior can be seen with the free play addition.

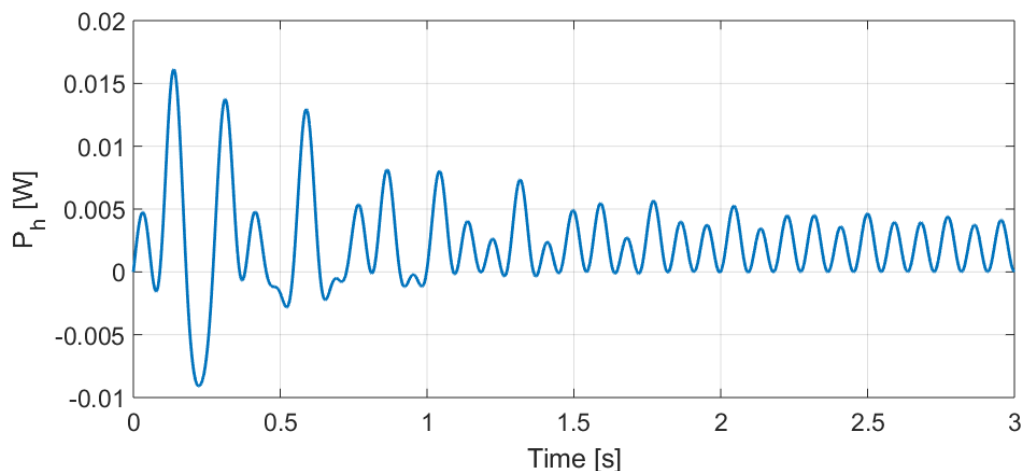


Figure 6.8 Power flowing from the mechanical to the electrical domain for at numerical short-circuit flutter speed (9.5 m/s)

Simulations and wind tunnel tests for both linear and nonlinear typical sections demonstrated that the piezoelectric based NES is able to slightly expand the flutter boundary. The comparison between numerical and experimental data had some issues regarding the prediction of flutter speed. Table 7 displays the obtained flutter speeds for the linear typical section and the range speeds in which LCO was observed for the nonlinear typical section.

Table 7. Comparison between speeds prediction

Case	Typical Section	Numerical flutter speed / LCO range	Experimental flutter speed / LCO range	Error (experimental and numerical)
SC	Linear	9.8 m/s	10.8 m/s	10.2 %
NES	Linear	10.1 m/s (+3.1%)	11.2 m/s (+3.7 %)	10.9 %
SC	Nonlinear	9.5 m/s - 9.8 m/s	11.0 m/s	14.0 %
NES	Nonlinear	9.9 m/s (+2.6 %)	11.3 m/s (+2.5 %)	13.8 %

The short-circuit case is equivalent to an electromechanically uncoupled system since the change in the piezoelectric material stiffness can be neglected in this condition. In this context, we can assume the mechanical system (or the equivalent electrical circuit) is responsible for the difference between numerical and experimental results (10.2 % for the linear and 14.0 % for the nonlinear typical section) for the SC condition. Considering the limitations of the numerical model (e.g. Theodorsen's theory limitations, assumptions and simplifications), the inaccuracies of the experimental data (e.g. typical section nonlinearities, experimental identification of parameters, wind speed measurement and variation during tests) the error between the experimental and numerical short circuit flutter speed is tolerable. The error is higher for the nonlinear typical section in both SC and NES configurations. It can be caused by the need to perform the experiments with a higher initial condition in order to trigger the LCO. Since nonlinear energy sinks are sensitive to the initial condition (CATALDO; BELLIZZI; SAMPAIO, 2013) and the experimental initial condition is set manually, the addition of the piezoelectric based NES to the linear typical is expected to increase the error, especially in the transient region. In accordance with it, the error increased from 10.2 % to 10.9 %.

The nonlinear typical section behaved contrary to expectations and the addition of the NES decreased the error from 14.0 % to 13.8 %. However, while the reference case presented a range of LCO, when connected to the NES, the nonlinear typical section, as in the linear case, presents a critical speed in which changes from stable to unstable.

## 7 Conclusions

This work extends the use of piezoelectric based nonlinear absorbers to aeroelastic problems. In particular, it investigates numerically and experimentally the effects of a piezoelectric based energy sink device on the aeroelastic behavior of linear and nonlinear typical sections. An equivalent electrical circuit was considered for both typical section cases in the simulations. The essentially nonlinear piezoelectric shunt combines a resistor, an inductor a negative capacitance and a nonlinear capacitance all connected in series. First, simulations with the piezoelectric based NES were performed to verify the levels of the voltage across the piezoelectric material. In this part, the need of a high voltage operational amplifier for the experimental setup was identified.

Secondly, the effects of different NES parameters on control performance of the linear typical section were verified and a set of parameters that results in enhanced vibration suppression determined. In this step, the parameters were set so that the voltages across the piezoelectric material electrodes is limited. Then, the aeroelastic behavior of the linear typical section in short-circuit condition was assumed as a reference case. The short-circuit flutter speed was determined and the change in the flutter speed due to the NES was verified numerically and experimentally. The behavior of the system is presented in time and frequency domain and energy exchanges are included. Lately, a concentrated nonlinearity, free play, was added to the typical section and the same analysis were performed for the new configuration.

The experimental results validate the modeling used (linear and nonlinear equivalent model) and the proposed NES circuit. Despite the differences between numerical and experimental results, displayed in Table 7, the piezoelectric based NES was able to slightly expand the flutter boundary for all cases, from 2.5 % for the nonlinear typical section to 3.7 % for the linear one, which is close to the increase obtained by Lee and his co-authors (LEE et al., 2007a, 2007b).

The high-voltage operational amplifier still is an important limiting factor for this work since numerical analysis demonstrated that the piezoelectric based NES could operate more effectively when allowed to operate with higher voltage. Another advantage of the piezoelectric circuit used is that, due to the versatility of the attachment, several nonlinear piezoelectric absorbers (and other nonlinearities, e.g. Duffing-type) can be achieved through simple modifications to the circuit presented in

Figure 4.3. In other words, polynomial nonlinearities of virtually any order can be obtained by excluding the negative capacitance and including more multipliers, yielding tuned nonlinear vibration absorbers discussed in the literature (SOLTANI; KERSCHEN, 2015).

## 8 References

ABDELKEFI, A. Aeroelastic energy harvesting: a review. **International Journal of Engineering Science**, v. 100, p. 112–135, 2016.

AGNENI, A. et al. Multi-modal damping by shunted piezo-patches: possible aeroelastic applications. **International Journal of Applied Electromagnetics and Mechanics**, v. 24, n. 1–2, p. 1–24, 2006.

AGNENI, A.; MASTRODDI, F.; POLLI, G. M. Shunted piezoelectric patches in elastic and aeroelastic vibrations. **Computers and Structures**, v. 81, n. 2, p. 91–105, 2003.

AHMADIAN, M.; DEGUILIO, A. P. Recent advances in the use of piezoceramics for vibration suppression. **Shock and Vibration Digest**, v. 33, n. 1, p. 15–22, 2001.

AL-SHUDEIFAT, M. A. et al. Numerical and experimental investigations of a rotating nonlinear energy sink. **Meccanica**, v. 52, n. 4–5, p. 763–779, 2017.

ALESSANDRONI, S. et al. A passive electric controller for multimodal vibrations of thin plates. **Computers and Structures**, v. 83, n. 15–16, p. 1236–1250, 2005.

ALESSANDRONI, S.; DELL'ISOLA, F.; PORFIRI, M. A revival of electric analogs for vibrating mechanical systems aimed to their efficient control by PZT actuators. **International Journal of Solids and Structures**, v. 39, n. 20, p. 5295–5324, 2002.

ANDREAUS, U.; DELL'ISOLA, F.; PORFIRI, M. Piezoelectric passive distributed controllers for beam flexural vibrations. **Journal of Vibration and Control**, v. 10, n. 5, p. 625–659, 2004.

BAYIK, B. et al. Equivalent circuit modeling of a piezo-patch energy harvester on a thin plate with AC-DC conversion. **Smart Materials and Structures**, 2016.

BECK, B. S.; CUNEFARE, K. A.; COLLET, M. The power output and efficiency of a negative capacitance shunt for vibration control of a flexural system. **Smart Materials and Structures**, v. 22, n. 6, 2013.

BEHRENS, S.; FLEMING, A. J.; MOHEIMANI, S. O. R. **New method for multiple-mode shunt damping of structural vibration using a single piezoelectric transducer**. Proceedings of SPIE - Smart Structures and Materials. **Anais...**2001

BISPLINGHOFF, R. L.; ASHLEY, H.; HALFMAN, R. L. **Aeroelasticity**. New York: Dover Publications, 1996.

CATALDO, E.; BELLIZZI, S.; SAMPAIO, R. Free vibrations of an uncertain energy pumping system. **Journal of Sound and Vibration**, v. 332, n. 25, p. 6815–6828, 2013.

D'ASSUNÇÃO, D.; DE MARQUI, C. Applied self-powered semi-passive control for a 2-degree-of-freedom aeroelastic typical section using shunted piezoelectric materials. **Journal of Intelligent Material Systems and Structures**, v. 26, n. 4, p. 373–385, 2015.

DEN HARTOG, J. P. **Mechanical vibrations**. [s.l: s.n.].

DOWELL, E. H. **A modern course in aeroelasticity**. 5. ed. [s.l.] Springer, 2015. v. 217

DOWELL, E. H.; TANG, D. Nonlinear aeroelasticity and unsteady aerodynamics. **AIAA Journal**, 2002.

ELVIN, N. G. Equivalent electrical circuits for advanced energy harvesting. **Journal of Intelligent Material Systems and Structures**, v. 25, n. 14, p. 1715–1726, 2014.

ELVIN, N. G.; ELVIN, A. A. A general equivalent circuit model for piezoelectric generators. **Journal of Intelligent Material Systems and Structures**, v. 20, n. 1, p. 3–9, 2009a.

ELVIN, N. G.; ELVIN, A. A. A coupled finite element-circuit simulation model for analyzing piezoelectric energy generators. **Journal of Intelligent Material Systems and Structures**, 2009b.

ERTURK, A.; INMAN, D. J. An experimentally validated bimorph cantilever model for piezoelectric energy harvesting from base excitations. **Smart Materials and Structures**, v. 18, n. 2, p. 025009, 2009.

FORWARD, R. L. Electronic damping of vibrations in optical structures. **Applied Optics**, v. 18, n. 5, p. 690–697, 1979.

GENDELMAN, O. V. Transition of energy to a nonlinear localized mode in a highly asymmetric system of two oscillators. **Nonlinear Dynamics**, v. 25, n. 1–3, p. 237–253, 2001.

GENDELMAN, O. V. et al. Energy pumping in nonlinear mechanical oscillators: part I - dynamics of the underlying hamiltonian systems. **Journal of Applied Mechanics**, v. 68, n. 1, p. 34, 2001.

HABIB, G. et al. Nonlinear generalization of Den Hartog's equal-peak method. **Mechanical Systems and Signal Processing**, v. 52–53, n. 1, p. 17–28, 2015.

HABIB, G.; KERSCHEN, G. A principle of similarity for nonlinear vibration absorbers. **Physica D: Nonlinear Phenomena**, v. 332, p. 1–8, 2016.

HAGOOD, N. W.; CRAWLEY, E. F. Experimental investigation of passive enhancement of damping for space structures. **Journal of Guidance, Control, and Dynamics**, v. 14, n. 6, p. 1100–1109, 1991.

HAGOOD, N. W.; VON FLOTOW, A. Damping of structural vibrations with piezoelectric materials and passive electrical networks. **Journal of Sound and Vibration**, v. 146, n. 2, p. 243–268, 1991.

HODGES, D. H.; PIERCE, G. A.; CUTCHINS, M. A. **Introduction to structural dynamics and aeroelasticity**. [s.l: s.n.]. v. 56

HUBBARD, S. A. et al. Targeted energy transfer between a model flexible wing and nonlinear energy sink. **Journal of Aircraft**, v. 47, n. 6, p. 1918–1931, nov. 2010.

HUBBARD, S. A. et al. Transonic aeroelastic instability suppression for a swept wing by targeted energy transfer. **Journal of Aircraft**, v. 51, n. 5, p. 1467–1482, 2014.

JONES, D. I. G. **Handbook of viscoelastic vibration damping**. [s.l.] J. Wiley,

2001.

LEE, Y. S. et al. Triggering mechanisms of limit cycle oscillations due to aeroelastic instability. **Journal of Fluids and Structures**, v. 21, n. 5–7, p. 485–529, dez. 2005.

LEE, Y. S. et al. Suppressing aeroelastic instability using broadband passive targeted energy transfers, part 2: experiments. **AIAA Journal**, v. 45, n. 10, p. 2391–2400, 2007a.

LEE, Y. S. et al. Suppressing aeroelastic instability using broadband passive targeted energy transfers, part 1: theory. **AIAA Journal**, v. 45, n. 3, p. 693–711, mar. 2007b.

LEO, D. J. L. **Engineering analysis of smart material systems**. [s.l: s.n.].

LESIEUTRE, G. A. Vibration damping and control using shunted piezoelectric materials. **Shock and Vibration Digest**, v. 30, n. 3, p. 187–195, 1998.

MCFARLAND, D. M.; BERGMAN, L. A.; VAKAKIS, A. F. Experimental study of non-linear energy pumping occurring at a single fast frequency. **International Journal of Non-Linear Mechanics**, v. 40, n. 6, p. 891–899, jul. 2005.

MCGOWAN, A. R. **An examination of applying shunted piezoelectrics to reduce aeroelastic response** CEAS/AIAA/ICASE/NASA Langley International Forum on Aeroelasticity and Structural Dynamics, 1999.

MOON, F. C. Chaotic vibrations. **IEEE Power Engineering Review**, 1985.

NASHIF, A. D.; JONES, D. I. G.; HENDERSON, J. P. **Vibration damping**. [s.l.] Wiley, 1985.

NAYFEH, A. H.; MOOK, D. T. **Nonlinear oscillations**. [s.l: s.n.].

SILVA, T. M. P. et al. Effects of a piezoelectric based nonlinear energy sink on the behavior of an electromechanically coupled beam. **Active and Passive Smart Structures and Integrated Systems XII**, v. 1059509, n. March, p. 7, 2018.

SILVA, T. M. P.; CLEMENTINO, M. A.; DE MARQUI, C. An experimentally validated piezoelectric nonlinear energy sink for wideband vibration attenuation. **Journal of Sound and Vibration**, v. 437, p. 68–78, 2018.

SOLTANI, P.; KERSCHEN, G. The nonlinear piezoelectric tuned vibration absorber. **Smart Materials and Structures**, v. 24, n. 7, p. 75015, 2015.

THEODORSEN, T. **General theory of aerodynamic instability and the mechanism of flutter** NACA Report. [s.l: s.n.].

UCHINO, K.; ISHII, T. Mechanical damper using piezoelectric ceramics. **Nippon Seramikkusu Kyokai Gakujutso Ronbunshi - Journal of the Ceramic Society of Japan**, v. 96, n. 8, p. 863–867, 1988.

VAKAKIS, A. F. et al. **Nonlinear targeted energy transfer in mechanical and structural systems**. [s.l: s.n.]. v. 156

VAKAKIS, A. F.; GENDELMAN, O. V. Energy pumping in nonlinear mechanical oscillators: part II - resonance capture. **Journal of Applied Mechanics**, v. 68, n. 1, p. 42, 2001.

VIGUIÉ, R.; KERSCHEN, G.; RUZZENE, M. **Exploration of nonlinear**

**shunting strategies as effective vibration absorbers.** Proceedings of SPIE - Active and Passive Smart Structures and Integrated Systems. **Anais...**2009

WU, S. Piezoelectric shunts with a parallel R-L circuit for structural damping and vibration control. **Spie**, v. 2720, n. Lc, p. 259–269, maio 1996.

WU, S. **Piezoelectric shunt vibration damping of an F-15 panel under high-acoustic excitation.** Proceedings of SPIE. **Anais...**2000

YAMADA, K. et al. Optimum tuning of series and parallel LR circuits for passive vibration suppression using piezoelectric elements. **Journal of Sound and Vibration**, v. 329, n. 24, p. 5036–5057, 2010.

ZHOU, B.; THOUVEREZ, F.; LENOIR, D. Essentially nonlinear piezoelectric shunt circuits applied to mistuned bladed disks. **Journal of Sound and Vibration**, v. 333, n. 9, p. 2520–2542, 2014.

## Appendix A - Identification of Typical Section Parameters

The airfoil semichord is 0.125 m. Despite the physical length of the airfoil, the assumed value is 0.5 m, since it corresponds to the size of the wind tunnel nozzle. The airfoil shaft is placed on the aerodynamic center, which is found at 25 % of the airfoil chord line ( $a = -0.5$ ). The airfoil mass is 0.804 kg. The mass of the fixtures that attach the airfoil to the stationary frame is 1.060 kg. The total mass that translates is assumed as the sum of these two masses. It is important to note that the contribution of the four beams in the translational mass is not being considered. The CG is determined by equilibrating the typical section on a 1 mm-thick beam and measuring the distance between the mean thickness of that beam and the center of the elastic axis in 25.8 mm ( $x_\alpha = 0.2064$ ). The moment of inertia is determined using the pendulum equation:

$$T_\alpha = 2\pi \sqrt{\frac{I_\alpha l}{mgx_\alpha b}} \quad (10.1)$$

where  $T_\alpha$  is the period of oscillation and  $g$  is the gravity acceleration ( $9.7876 \text{ m.s}^{-2}$ ). The ends of the shaft are supported so that the typical section stays horizontally in a free-to-rotate condition. An arbitrary input angle is applied, and the oscillation is measured. The period of oscillation is determined as 0.7413 s, resulting in a moment of inertia equal to  $2.8 \text{ g.m}^2$ .

As mentioned, the plunge stiffness is due to the four elastic beams, so, the plunge stiffness is estimated by two methods: first through the theoretical beam stiffness and through static displacement experiments. The equation for a beam with no distributed loads:

$$YI_z \frac{d^4 w_y(x)}{dx^4} = 0 \quad (10.2)$$

where  $Y$  is the Young's modulus,  $I_z$  is the moment of inertia and  $u_y$  is the transversal displacement. Integrating four times:

$$YI_z \frac{d^3 u_y(x)}{dx^3} + k_1 = 0 \quad (10.3)$$

$$YI_z \frac{d^2 u_y(x)}{dx^2} + k_1 x + k_2 = 0 \quad (10.4)$$

$$YI_z \frac{du_y(x)}{dx} + \frac{k_1}{2}x^2 + k_2x + k_3 = 0 \quad (10.5)$$

$$YI_z u_y(x) + \frac{k_1}{6}x^3 + \frac{k_2}{2}x^2 + k_3x + k_4 = 0 \quad (10.6)$$

knowing that the shear force  $V_y$ , bending moment  $M_z$  and rotation  $\theta_z$  of the transverse section can be calculated as:

$$\frac{dM_z(x)}{dx} = V_y(x) = YI_z \frac{d^3u_y(x)}{dx^3} \quad (10.7)$$

$$M_z(x) = YI_z \frac{d^2u_y(x)}{dx^2} \quad (10.8)$$

$$\theta_z(x) = YI_z \frac{du_y(x)}{dx} \quad (10.9)$$

and applying the boundary conditions:

$$u_y(0) = 0 \rightarrow k_4 = 0 \quad (10.10)$$

$$\theta_z(0) = 0 \rightarrow k_3 = 0 \quad (10.11)$$

$$\theta_z(L_{beam}) = 0 \rightarrow k_2 = -\frac{k_1 L_{beam}}{2} \quad (10.12)$$

$$V_y(L_{beam}) = -P_y \rightarrow k_1 = P_y \quad (10.13)$$

the tip displacement can be calculated by:

$$u_y(L_{beam}) = \frac{P_y L_{beam}^3}{12YI_z} \quad (10.14)$$

which means the single beam stiffness is:

$$K_{beam} = \frac{P_y}{u_y} = \frac{12YI_z}{L_{beam}^3} = \frac{12Y \left( \frac{b_{beam} h_{beam}^3}{12} \right)}{L_{beam}^3} = \frac{Y b_{beam} h_{beam}^3}{L_{beam}^3}. \quad (10.15)$$

Using the beam parameters of Table 8, and assuming the system stiffness is four times the beam stiffness, the resulting value is 2100 N/m. This method does not consider the stiffness of the piezoelectric material.

Table 8. Beam parameters

Parameter	Value
Y	210 GPa
$L_{\text{beam}}$	200 mm
$b_{\text{beam}}$	20 mm
$h_{\text{beam}}$	1 mm

The experimental determination of the stiffness by using the static displacement method considers a spring-mass system. A scheme with pulleys and nylon rope is used to support weights. A linear fitting is obtained from the static displacement curve from applied load. A similar experimental process is performed to determine the pitch stiffness.

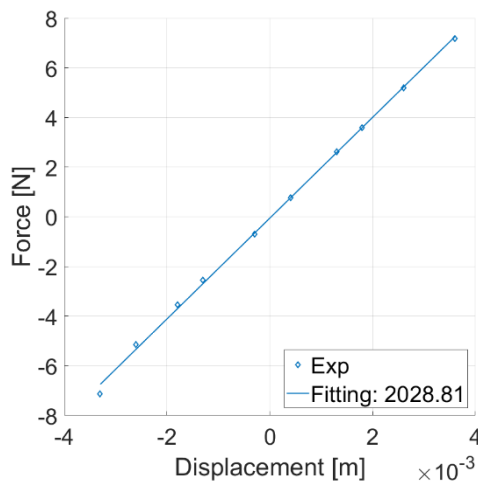


Figure A.0.1 Plunge Stiffness

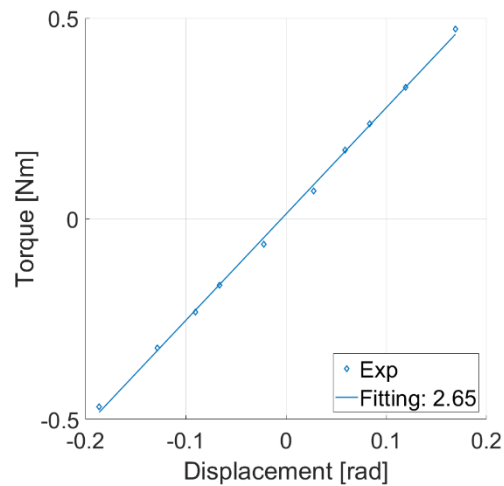


Figure A.0.2 Pitch Stiffness

These tests are also useful for verifying the linearity of the springs. Different from what expected, the plunge stiffness is lower than the theoretical beam stiffness. Wind tunnel tests indicates that the value of 2100 N/m results in better representation of the plunge frequency for the reference case, so it is assumed as the plunge stiffness final value.

The damping is obtained from the free response of each DOF, with the other one locked. Assuming that the response can be written as:

$$u(t) = e^{-\xi\omega_n t} \quad (10.16)$$

an exponential fitting for the envelope curve is used to calculate the damping factors  $\xi_h$  and  $\xi_\alpha$ .

$$u(t) = ae^{bt}. \quad (10.17)$$

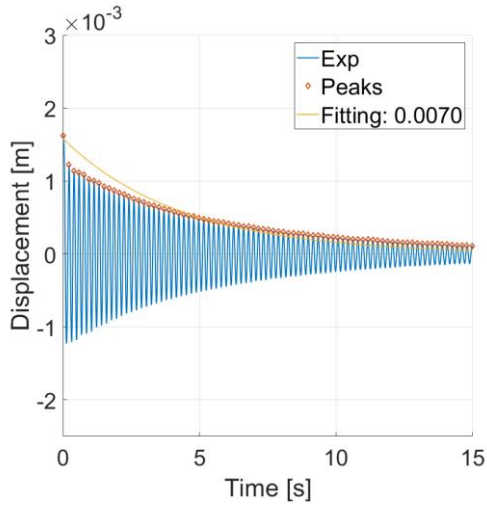
Then, the damping factors can be calculated using the natural frequencies:

$$\xi_h = -b \sqrt{\frac{(m + m_f + m_{f \text{ damp}})}{K_h}} \quad (10.18)$$

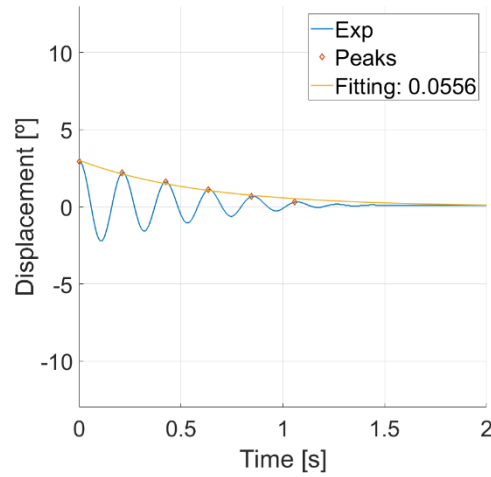
$$\xi_\alpha = -b \sqrt{\frac{I_\alpha}{K_\alpha}} \quad (10.19)$$

where  $m_{f \text{ damp}}$  is the mass of the device used to lock the pitch DOF, which is 0.09 kg.

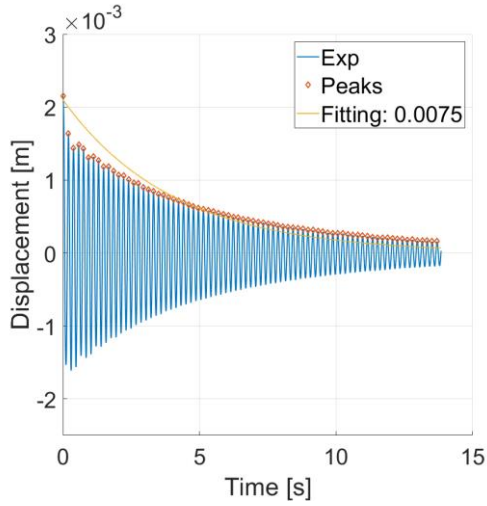
Three tests are performed for each DOF and the experimental curves are shown in Figure A.0.3 for plunge and Figure A.0.4 for pitch.



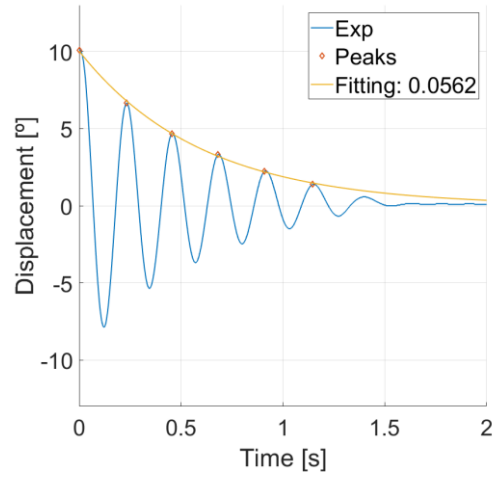
(a)



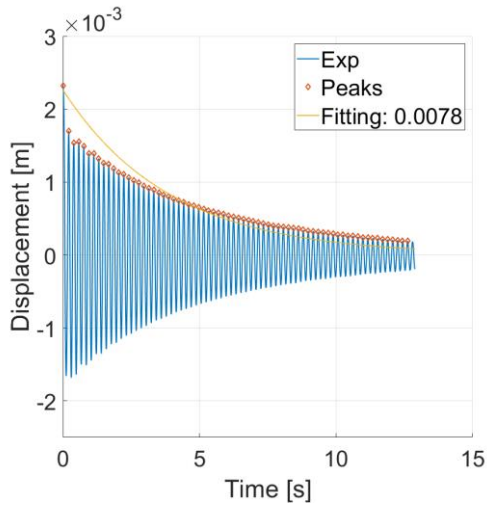
(a)



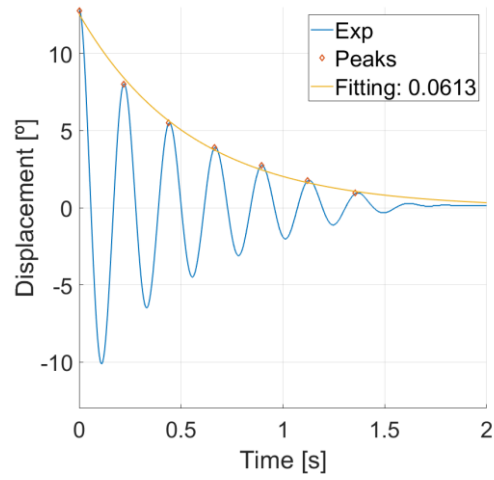
(b)



(b)



(c)



(c)

Figure A.0.3 Plunge Damping

Figure A.0.4 Pitch Damping

For plunge, one can note the initial condition does not follow the envelope curve. To consider it in the simulation, the exponential fitting considers a higher weight for the first point, so that the fitted curve (yellow) starts in the initial condition. The damping factors are assumed as the medium value between the three curve fittings or 0.0075 for plunge and 0.0577 for pitch. Then, the damping coefficient is calculated from:

$$B_h = 2\xi_h \sqrt{K_h(m + m_f)} \quad (10.20)$$

$$B_\alpha = 2\xi_\alpha \sqrt{K_\alpha I_\alpha} . \quad (10.21)$$

The final values for damping coefficients are 1.877 N.s/m for plunge and 0.0199 N.m.s/rad for pitch.